

Detecting active latitudes of Sun-like stars using asteroseismic a-coefficients

Othman Benomar¹²³, Masao Takata⁴, Michael Bazot⁵, Takashi Sekii¹², Laurent Gizon³⁶⁷, and Yuting Lu⁸

¹ Department of Astronomical Science, School of Physical Sciences, SOKENDAI, 2-21-1 Osawa, Mitaka, Tokyo 181-8588 e-mail: othman.benomar@nao.ac.jp, ob19@nyu.edu

² Solar Science Observatory, National Astronomical Observatory of Japan, 2-21-1 Osawa, Mitaka, Tokyo 181-8588, Japan

³ New York University Abu Dhabi, Center for Space Science, PO Box 129188, UAE

⁴ Department of Astronomy, School of Science, The University of Tokyo, 7-3-1 Hongo, Bunkyo-ku, Tokyo, 113-0033, Japan

⁵ Heidelberg Institut für Theoretische Studien, Schloss-Wolfsbrunnenweg 35, 69118 Heidelberg, Germany

⁶ Max-Planck-Institut für Sonnensystemforschung, 37077, Göttingen, Germany

⁷ Institut für Astrophysik, Georg-August-Universität Göttingen, 37077, Göttingen, Germany

⁸ Department of Physics, The University of Tokyo, Tokyo 113-0033, Japan

Received 30 May 2023 Accepted August 16, 2023

ABSTRACT

Aims. We introduce a framework to measure the asphericity of Sun-like stars using a_1 , a_2 and a_4 coefficients, and constrain their latitudes of magnetic activity.

Methods. Systematic errors on the inferred coefficients are evaluated in function of key physical and seismic parameters (inclination of rotation axis, average rotation, height-to-noise ratio of peaks in power spectrum). The measured a-coefficients account for rotational oblateness and the effect of surface magnetic activity. We use a simple model that assumes a single latitudinal band of activity.

Results. Using solar SOHO/VIRGO/SPM data, we demonstrate the capability of the method to detect the mean active latitude and its intensity changes between 1999-2002 (maximum of activity) and 2006-2009 (minimum of activity). We further apply the method to study the solar-analogue stars 16 Cyg A and B using Kepler observations. An equatorial band of activity, exhibiting intensity that could be comparable to that of the Sun, is detected in 16 Cyg A. However, 16 Cyg B exhibits a bi-modality in a_4 that is challenging to explain. We suggest that this could

be a manifestation of the transition between a quiet and an active phase of activity. Validating or invalidating this hypothesis may require new observations.

Key words. stars:activity, stars:rotation, stars:solar-type, asteroseismology

1. Introduction

The observations from the space-borne instruments MOST (Walker et al. 2003), CoRoT (Baglin et al. 2006), *Kepler* (Borucki et al. 2010) and TESS (Ricker et al. 2014) have been important in advancing our knowledge of stellar interiors. This is particularly true for *Kepler*, which could observe continuously tens of thousand of stars for nearly four continuous years, enabling asteroseismic measurements that almost rival disk-integrated helioseismic measurements from a decade ago. Those precise measurements have for example enabled us to better understand stellar rotation and its impact on stellar evolution. The asteroseismology of Sun-like stars is based on the study of the pressure modes that are excited by turbulent convection in the outer layers of these stars. The acoustic modes may reach deep into the core or may be localised close to the stellar surface, giving access to the internal structure and dynamics of the stars. Rotation has a critical impact on the stellar structure and evolution as it induces a material mixing process (Maeder & Meynet 2008). Rotation is also an essential ingredient of the dynamo-effect (Thompson et al. 2003) and can lead to a distortion of the star's shape due to the centrifugal force (Chandrasekhar 1969). For fast rotators, the rotational flattening must be taken into account. These stars show a variety of pulsation modes that are not present in slower rotators (e.g. Lignières et al. 2006).

Despite its slow rotation rate, the solar asphericity can be measured by helioseismology. While the Sun is seen as oblate by acoustic modes during the quiet phases of its activity cycle, the modes feel a more complicated shape during activity maxima. During solar maxima, the frequencies of acoustic modes increase slightly due to the presence of active regions. The perturbation occurs near the surface and is stronger for modes that sense the active latitudes (below $\approx 30^\circ$ for the Sun). Physically the magnetic perturbations consist of several components that are not easy to disentangle (incl. stratification and wave speed perturbations (Libbrecht & Woodard 1990; Antia et al. 2000; Dziembowski et al. 2000). The magnetic perturbations affect the acoustic modes near the surface over only a few hundred kilometres, that is of order $10^{-5} R_\odot$, but is significant enough to be measured.

The origin of stellar activity is not well understood as it depends on the complex interplay between rotation, convection and the magnetic field (Brun & Browning 2017). Stellar magnetic cycles are observed in most cool stars (Simon et al. 2002) over a large range of the electromagnetic spectrum and evidence of activity cycles is observed in X-ray (eg. Catura et al. 1975), radio waves (White 1999; White et al. 2017), chromospheric emission lines (Vaughan 1983; Oláh et al. 2009, 2016), and also through luminosity variation due to surface magnetic activity in the visible (Hartmann & Rosner 1979; Silva-Valio et al. 2010; Ceillier et al. 2017). On Sun-like stars, the

level of activity is often observed to be cyclic, with activity periods ranging from a few years to decades. Although there are relationships between the stellar age, the rotation period, and the level of activity (van Saders et al. 2016), the underlying mechanisms at play are not understood.

Since the advent of space-borne photometry and the observation of Sun-like pulsators by CoRoT, it became evident that helioseismic methods used for the Sun may be applied to asteroseismic observations. This has resulted in robust estimates of the average rotational splittings, which, in combination with the surface rotation rates inferred from photometric variability, indicate that main sequence stars have nearly-uniform internal rotation rates, (Gizon et al. 2013; Benomar et al. 2015; Nielsen et al. 2017). All of the recent seismic studies of radial differential rotation agree that angular momentum transport in the radiative zone is much more efficient than considered in theory, even in the case of stars more massive than Sun-like stars, such as γ -Doradus stars (eg. Mosser et al. 2012; Gehan et al. 2018; Ouazzani et al. 2019). For the best Kepler observations, asteroseismology showed evidence of latitudinal differential rotation for main sequence stars (Benomar et al. 2018a) and of the radial differential rotation in RGB (e.g. Deheuvels et al. 2012, 2014).

This paper aims at providing a framework to study stellar activity and its latitude by analysing its effect on pulsation frequencies. The proposed method involves the use of the a -coefficient decomposition (Schou et al. 1994; Pijpers 1997, 1998) on the stellar power spectrum, conveniently separating the perturbations caused by rotation and asphericity. The method is tested on Sun-as-a-star data and on the solar-analogues 16 Cyg A and B, which are the two brightest stars in the initial Kepler observation field.

Only few successful measurements of the asphericity of other stars than the Sun have been made so far. Using ultra-precise measurements of the frequency splittings of time-harmonic (i.e. non-stochastic) low-degree p-modes, Gizon et al. (2016) inferred the oblateness of the γ Doradus– δ Scuti star KIC 11145123 to be $\Delta R = (1.8 \pm 0.6) \times 10^{-6} R \simeq 3 \pm 1$ km, i.e. smaller than expected from rotational oblateness alone, suggesting the presence of magnetic activity at low latitudes. Bazot et al. (2019) measured the asphericity of the solar-like pulsators 16 Cyg A and B and found that 16 Cyg A is likely prolate, implying that this star may have low-latitude magnetic activity on its surface.

In the spirit of the study by Gizon (2002), we will perform monte-carlo simulations to demonstrate the possibility of inferring the even- a coefficients from simulated oscillation power spectra to constrain the latitude of activity. Unlike Gizon (2002) who included only the a_2 coefficient in the parametric model, we will infer both the a_2 and a_4 coefficients. We start in Section 2 by introducing the effects of rotation on pulsation frequencies and discuss the effect of the centrifugal force and of the activity on the mode cavities. Section 3 presents the assumptions required for the asteroseismic measurement of stellar activity. Section 4 discusses the achievable accuracy of the seismic observables, while sections 5 and 6 present the results on solar data and for 16 CygA and B. This is followed by a discussion and conclusion in section 7.

71 2. The effect of rotation and of magnetic activity

72 This section presents the effect of rotation and of magnetic activity on pulsation modes, and intro-
 73 duces the frequency model used for asteroseismic data analysis.

74 2.1. Frequency splittings

75 Slowly rotating stars without significant magnetic activity are approximately spherical and it is
 76 common to describe the family of modes travelling inside it using spherical harmonics (see e.g.
 77 Unno et al. 1989). If the departure from spherical shape remains small enough, it is convenient to
 78 keep the spherical representation for the equilibrium model and account for distortions through a
 79 perturbation analysis. All pulsations can then be described using a set of integers (n,l,m) , namely
 80 the radial order, the mode degree and the azimuthal order, respectively. Acoustic pressure modes
 81 observed in Sun-like stars can be identified using their frequencies ν_{nlm} .

82 In a non-rotating, non-active star, m-components are degenerate and cannot be resolved. When
 83 rotation or magnetic activity sets in, this degeneracy is lifted. The resulting frequency is treated as
 84 a perturbation to the degenerate frequency without rotation and activity,

$$\nu_{nlm} = \nu_{nl} + \delta\nu_{nlm}, \quad (1)$$

85 with ν_{nl} , the equilibrium eigenfrequency without rotation and activity and $\delta\nu_{nlm}$ the frequency split-
 86 ting. These splitting may depend on multiple physical effects perceived by the modes (Libbrecht
 87 & Woodard 1990) within their cavity of propagation. These can be terms of order $O(\Omega)$, with Ω
 88 the rotation rate estimated at the equator, $\Omega = \Omega(r, \theta = \pi/2)$. These depend directly on the stellar
 89 rotation profile $\Omega(r, \theta)$. Higher-order perturbations pertaining to the shape of the mode cavity can
 90 also exist. Note that ν_{nl} differs from $\nu_{nl, m=0}$ as the $m = 0$ components may have their frequency
 91 shifted by perturbations such as the magnetic activity (see e.g. Figure 1).

92 Splitting can be described using the Clebsch-Gordan a-coefficient decomposition (Ritzwoller
 93 & Lavelle 1991), that corresponds to a representation of the splittings on a basis of polynomials
 94 $\mathcal{P}_j^{(l)}(m)$ of degree j in m ,

$$\delta\nu_{nlm} = \sum_{j=1}^{j_{max}} a_j(n, l) \mathcal{P}_j^{(l)}(m), \quad (2)$$

95 with the polynomials such that

$$\sum_{m=-l}^l \mathcal{P}_i^{(l)}(m) \mathcal{P}_j^{(l)}(m) = 0 \text{ when } i \neq j. \quad (3)$$

96 Here, $a_j(n, l)$ is the a-coefficient of order j and $j_{max} = 2l$ is the maximum order to which the
 97 decomposition must be carried for a given degree. The standard set of polynomials used in this
 98 expansion are those normalised as per described by Schou et al. (1994).

This decomposition is extensively used in helioseismology and was used on Sun-like stars by Benomar et al. (2018a). Asteroseismology has been so far unable to observe modes of degree higher than $l = 3$ so that in the following the discussion is restricted to $l \leq 3$ and $j_{max} = 2l = 6$, due to the selection rule of the $\mathcal{P}_j^{(l)}(m)$. This limitation is the consequence of full-disk integrated photometric observations. An example of splitting including odd and even a_j coefficients is given in Figure 1 for $l = 1, 2$.

This theoretical model leads to a natural interpretation of the observed splittings. One may decomposes these latter into their symmetrical, S_{nlm} , and anti-symmetrical, T_{nlm} , parts. These components can then be described as sums over, respectively, the odd and even a-coefficients,

$$S_{nlm} = \frac{\nu_{n,l,m} - \nu_{n,l,-m}}{2m} = \frac{1}{m} \sum_{j=1}^{j_{max}/2} a_{2j-1}(n, l) \mathcal{P}_{2j-1}^{(l)}(m), \quad (4)$$

$$T_{nlm} = \frac{\nu_{n,l,m} + \nu_{n,l,-m}}{2} - \nu_{n,l,0} = \sum_{j=1}^{j_{max}/2} a_{2j}(n, l) (\mathcal{P}_{2j}^{(l)}(m) - \mathcal{P}_{2j}^{(l)}(0)). \quad (5)$$

This arises from the parity relation $\mathcal{P}_j^{(l)}(-m) = (-1)^j \mathcal{P}_j^{(l)}(m)$. These equations can be used to express the a-coefficients with S_{nlm} and T_{nlm} . They also provide relations between the ν_{nlm} with the $a_j(n, l)$ (Appendix A.2).

It can be seen from Appendix A.1 that the sums in Eqs. (4) and (5) involve, respectively, odd and even functions of m . Physically, this means that the symmetrical components of the splittings (Gough & Thompson 1990) result from large-scale perturbations sensitive to the prograde or retrograde nature of the waves, such as advection or the Coriolis force. On the other hand, the anti-symmetric splittings are caused by processes that are not affected by the propagation direction of waves. This may include the centrifugal force, that scales as $O(\Omega^2)$, and whose effect on the oscillation frequencies varies as m^2 . Magnetic fields or non-spherical deformations of the equilibrium structure will also contribute to the anti-symmetric splittings.

We further decompose the anti-symmetric splittings into a term depending on centrifugal-force-induced distortions and another one accounting for activity-related distortions,

$$T_{nlm} = \delta\nu_{nlm}^{(CF)} + \delta\nu_{nlm}^{(AR)}. \quad (6)$$

The symmetric part of the splitting corresponds to a term $\delta\nu_{nlm}^{(rot)}$ that stems from perturbations of order $O(\Omega)$ and the total observed splitting is,

$$\delta\nu_{nlm} = \delta\nu_{nlm}^{(rot)} + \delta\nu_{nlm}^{(CF)} + \delta\nu_{nlm}^{(AR)}. \quad (7)$$

Using the Sun as an archetype of Sun-like star, it is possible to measure these contributions to $\delta\nu_{nlm}$ as shown in Sections 2.2 and 2.3.

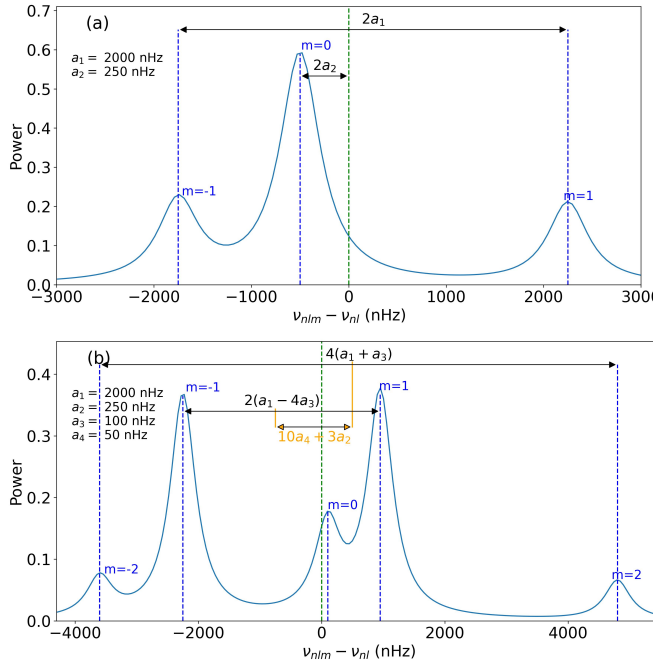


Fig. 1. Example of Lorentzian mode profiles showing the a-coefficients and their relationship with frequency spacings for $l = 1$ (a) and $l = 2$ modes (b). The orange spacing is $T_{n22} - T_{n21}$. v_{nl} is the m-averaged frequency of each multiplet. The stellar inclination is 40° .

125 2.2. Expressions for $\delta\nu_{nlm}^{(rot)}$, $\delta\nu_{nlm}^{(CF)}$ and $\delta\nu_{nlm}^{(AR)}$

126 To the first order, the perturbation on the frequency due to rotation is,

$$\delta\nu_{nlm}^{(rot)} = \frac{m}{2\pi} \int_0^R \int_0^\pi K_{nlm}(r, \theta) \Omega(r, \theta) r dr d\theta, \quad (8)$$

127 where R is the radius of the star and the kernel $K_{nlm}(r, \theta)$ (Hansen et al. 1977) expresses the sensitivity of a mode to the rotation at the radial point r and co-latitude θ . $\Omega(r, \theta)$ is the rotation profile of the star. It can be shown that $\delta\nu_{nlm}^{(rot)}$ actually only depends on symmetrical splittings (Ritzwoller & Lavey 1991) which in turns depend only on odd coefficients. For example and for $l = 3$, it is expressed as,

$$\delta\nu_{nlm}^{(rot)} \simeq \mathcal{P}_1^{(l)}(m) a_1 + \mathcal{P}_3^{(l)}(m) a_3 + \mathcal{P}_5^{(l)}(m) a_5. \quad (9)$$

132 Centrifugal forces typically distort a spherical rotating sphere of gas into an oblate ellipsoid, 133 elongated at the equator. Functional analysis shows that the contribution of centrifugal forces to 134 the mode splitting scales with $\Omega^2 R^3 / GM$. Properly integrating higher-order terms of the perturbation 135 expansion over the aspherical volume of the star and using asymptotic expressions for the 136 equilibrium mode eigenfunctions (assuming n is large enough), leads to the following expression 137 for the centrifugal-force component of the frequency splitting (Gough & Taylor 1984; Gough & 138 Thompson 1990),

$$\delta\nu_{nlm}^{(CF)} = \frac{\Omega^2 R^3}{GM} v_{nl} Q_{lm}, \quad (10)$$

with $Q_{lm} \approx \frac{2}{3} \frac{l(l+1)-3m^2}{(2l-1)(2l+3)}$ factor depending on the density. Equation (10) means that 139

$$\delta\nu_{nlm}^{(CF)} = \mathcal{P}_2^{(l)}(m) a_2^{(CF)}(n, l) \quad (11)$$

with 140

$$a_2^{(CF)}(n, l) = -\frac{1}{2l+3} \frac{\Omega^2 R^3}{GM} \nu_{nl} \quad (12)$$

since $-(2l+3)Q_{lm} = \mathcal{P}_2^{(l)}(m)$. It should be noted that the contribution of the centrifugal-force-induced deformation to the frequency splittings can be described by a linear combination of the \mathcal{P}_{2j} polynomials (Gough & Taylor 1984; Gough & Thompson 1990). Since the stars are assumed to be slowly rotating, one may only retain terms of order $O(\Omega^2)$, which correspond to the contribution of the a_2 coefficient alone. 141
142
143
144
145

One can further approximate equation (12) in order to express $\delta\nu_{nlm}^{(CF)}$ as a function of quantities that can be obtained directly from the modelling of the acoustic power spectra of Sun-like stars (Benomar et al. 2018a). First, the stellar mean density of a Sun-like star scales to a good approximation with its large separation, that is the average distance in the frequency space between modes of identical degree and consecutive orders (Ulrich 1986). In solar units, this reads $\rho = (\rho_\odot / \Delta\nu_\odot) \Delta\nu$, with the solar density $\rho_\odot = (1.4060 \pm 0.0005) \times 10^3 \text{ kg m}^{-3}$ and $\Delta\nu_\odot = 135.20 \pm 0.25 \mu\text{Hz}$ (García et al. 2011b). With an accuracy estimated to a few percents for Sun-like stars (White et al. 2011), the use of this scaling relation is thought to be a decent approximation. 146
147
148
149
150
151
152
153

The second simplification uses the fact that the Clebsch-Gordan coefficient decomposition of the frequency splitting imposes a one-to-one relationship between the a-coefficients and the coefficients of the decomposition of the velocity field into poloidal and toroidal components (Ritzwoller & Lavey 1991). Helioseismology suggests that the Sun rotates with a near constant angular velocity down to at least $r/R_\odot = 0.2$ (e.g. Thompson et al. 2003), which is the maximum depth at which measurements from low-degree p modes are available. Furthermore, its outer-convective zone shows a differential rotation of $\simeq 30\%$ from the equator to the pole, which leads to an $a_{3,\odot}(n, l) \simeq 4 \text{ nHz}$ and to even smaller values for higher odds a-coefficients. This is significantly smaller than $a_{1,\odot}(n, l) \simeq 420 \text{ nHz}$. Therefore, the aforementioned one-to-one relation ensures that we can retain only the leading order in the expansion of the rotation rate and treat it as an average value, given in terms of seismic observables by $\Omega \simeq 2\pi a_1$. This leads to 154
155
156
157
158
159
160
161
162
163
164

$$a_2^{(CF)}(n, l) \simeq -\frac{\nu_{nl}}{2l+3} \frac{3\pi}{G\rho_\odot} \frac{\Delta\nu_\odot^2}{\Delta\nu^2} a_1^2. \quad (13)$$

165

Regarding $\delta\nu_{nlm}^{(AR)}$, there is no unambiguous theory to describe the effect of the near-surface magnetic activity on the shape of the cavity. Due to this and following Gizon (2002), a geometrical description is preferred to a physical model. This description assumes that the corresponding wave-speed perturbation separates in the latitudinal and radial coordinates. The proposed form of the 166
167
168
169

170 perturbation in frequency is,

$$\begin{aligned}\delta\nu_{nlm}^{(AR)} &= \nu_{nl}\epsilon_{nl} \int_0^{2\pi} \int_0^\pi F(\theta|\mathbf{x})|Y_l^m(\theta, \phi)|^2 \sin \theta d\theta d\phi \\ &= \nu_{nl}\epsilon_{nl}A_{lm}(\mathbf{x}) \\ &= \sum_{j=0}^{j_{\max}/2} \mathcal{P}_{2j}^{(l)}(m) a_{2j}^{(AR)}(n, l).\end{aligned}\quad (14)$$

171 The term $a_{2j}^{(AR)}(n, l)$ in equation (14) refers to the combined contribution of a magnetic field and
 172 other perturbations in the stellar structure (e.g. stratification, temperature). The geometrical weight
 173 function $A_{lm}(\mathbf{x})$ describes the effect of an active zone at the co-latitude θ , on a mode of degree
 174 l and azimuthal order m . $A_{lm}(\mathbf{x})$ is the product of two contributions. First, the normalised spher-
 175 ical harmonics $Y_l^m(\theta, \phi)$ that decompose the magnetic activity effect over each modes. These are
 176 spherical-polar coordinates defined in the inertial frame with a polar axis pointing in the direction
 177 of the rotation axis. Second, the weight distribution (or the shape of the active region) is defined by
 178 $F(\theta|\mathbf{x})$. Here, \mathbf{x} refers to the parameters that are necessary to describe the function $F(\theta|\mathbf{x})$.

179 On the Sun, large active regions persist on the surface for 1-2 rotation periods and are ran-
 180 domly distributed in longitude over well defined latitudes. Here we assume that the corresponding
 181 perturbation can be approximated by a function of latitude only. The general problem of distinct
 182 active regions on the differentially rotating surface would go beyond the present study (see Papini
 183 & Gizon 2019, for the case of a single long-lived active region). In this paper, we only consider
 184 perturbations that are approximately steady in the inertial frame (i.e. latitudinal bands of activity).

185 In theory, a third integral over the radius is necessary to describe the dependence of the mag-
 186 netic activity to the stellar depth. However, p modes are weakly sensitive to the deep structure
 187 inside stars. Here, the radial integral is replaced by ϵ_{nl} , the overall activity intensity. The frequency
 188 ν_{nl} allows a dimensionless ϵ_{nl} , that can be compared between stars. Section 3.2 further develops
 189 the required assumptions in order to obtain a reliable information content on the active region in
 190 asteroseismology.

191 2.3. Modelling the frequencies

192 Combining equation (1), (7), (8), (13) and (14) leads to,

$$\begin{aligned}\nu_{nlm} &= \nu_{nl} \left(1 + \frac{3\pi}{(2l+3)\mathcal{G}\rho_\odot} \frac{\Delta\nu_\odot^2}{\Delta\nu^2} a_1^2 \right) \\ &\quad + \epsilon_{nl}A_{lm}(\mathbf{x}) + \frac{m}{2\pi} \int_0^R \int_0^\pi K_{nlm}(r, \theta) \Omega(r, \theta) r dr d\theta.\end{aligned}\quad (15)$$

Using equation (1) and (2), ν_{nlm} can also be expressed using the a-coefficients without loss of generality. 193
generality. 194

$$\nu_{nlm} = \nu_{nl} + \sum_{j=1}^{2l} \mathcal{P}_j^{(l)}(m) a_j(n, l). \quad (16)$$

It is possible to use equation (15) in order to measure the activity parameters \mathbf{x} , by directly fitting the power spectrum. However, there are multiple benefits to use instead a two-step approach consisting in first using equation (16) for the fitting of the power spectrum to evaluate the a-coefficients (method detailed in Appendix B). And then, fitting the coefficients obtained during the first step, using solely the equations (13) and (14) (detailed in Appendix C). Firstly and in the general case, the evaluation of $A_{lm}(\mathbf{x})$ requires the precise computation of a double integral. This is a slow process, that increases the time necessary to fit the power spectrum¹. Postponing to an ulterior step the computation of $A_{lm}(\mathbf{x})$ reduces drastically the parameter space from a few tens of parameters to only a few², effectively making faster the convergence rate of the fitting algorithm and making it easier to explore the assumptions that have to be made on equation (15) in order to have a functional approach in real cases (see the discussions in Section 3). Secondly, it allows us to decouple the observables from the physics, enabling to test various physical assumptions without having to re-perform the lengthy power spectrum analysis. Finally, it eases the evaluation of the reliability of the activity determination, by enabling us to pinpoint the cause of biases (if any) on either the observables (eg. a_2 , a_4 , see Section 4) or on the interpretation of these observables in terms of physical parameters (see Section 3.3). The disadvantage of the two-step approach is that it requires more statistical assumptions, such as neglecting correlations and assuming Gaussian parameters. Although one can argue that it is possible to perform a hierarchical Bayesian analysis (eg. Hogg et al. 2010; Campante et al. 2016) to partly alleviate this issue, such an approach is generally slow and may cancel the benefits of the two-step approach. 214

3. Information content in low order a-coefficients

The general theoretical formulations of Section 2, demonstrate how pulsation frequencies are expressed as function of the rotation, the centrifugal distortion and the activity of stars. However, observational limitations need to be accounted to enable a viable, robust model that extract as much possible the information content within currently existing data. This necessarily requires additional assumptions, for which the rational is detailed hereafter. 220

3.1. Factors contributing to the splitting accuracy and precision

As explained in Kamiaka et al. (2018), the pulsation height (H) and the noise background (N) are important factors that reduce the capabilities of asteroseismic analyses. Those are a complex 222
223

¹Using a MCMC method, from a day to a couple of weeks for a single star on a present-day CPU

²With our choice of $A_{lm}(\mathbf{x})$, three parameters are fitted. See section 3.2.

function of the global stellar characteristics (mass, radius, age), of the convective motion at the surface of Sun-like stars, and also depend on the instrumental limitations. The mode height and the noise background are in fact difficult to evaluate *a priori*. However, the Height-to-Noise (HNR), defined as the ratio H/N can be used to assess the quality of the spectrum of a pulsation mode. In fact, Kamiaka et al. (2018) show that the HNR at maximum of mode height \widehat{HNR} , can be used to study biases on the stellar inclination. This is because all main sequence Sun-like stars show a similar dependency of the height and of the width as a function of the frequency (see e.g. Appourchaux et al. 2014). In Section 4, we propose the same, but on a-coefficients.

The \widehat{HNR} not only defines how many modes can be observed, but also the maximum degree of the modes that is observed. Considering specifically the Kepler observations, stars exhibit a \widehat{HNR} for $l = 0$ modes of up to 30, the highest HNR being observed for 16 Cyg A and 16 Cyg B. Kamiaka et al. (2018) showed that the capability of distinguishing rotationally split components is of great importance if one wants to obtain a reliable asteroseismic inference of the rotation characteristics and of the stellar inclination. In particular, the ratio $a_1/\Gamma_{v_{max}}$ between the a_1 coefficient and the mode width determined at the maximum of mode amplitude $\Gamma_{v_{max}}$ (see Figure 6), determines the expected bias on the stellar inclination. As shown in Section 4, $a_1/\Gamma_{v_{max}}$ also controls the importance of the bias for the other low order a-coefficients. Finally, another important factor is the spectrum resolution. The higher the resolution, the more resolved are the modes. Thus, observations T_{obs} of several years are the most suitable in order to resolve and measure rotationally split components. Broadly speaking, observations exceeding a year and $a_1/\Gamma > 0.4$ are preferable to ensure a reliable measurement of a_1 .

All of the limitations discussed above incite us to introduce assumptions to ensure robust measurements of a-coefficients (ie, mitigate biases).

3.2. Latitudinal profile of the activity

Noting that it is challenging to measure low-degree a-coefficients for the Sun (eg. Toutain & Kosovichev 2001), we present here a minimal set of assumptions on even a-coefficients allowing us to constrain the asphericity of stellar cavities. One of the first aspects that has to be considered is the form of $F(\theta|x)$, the function characterising the activity latitude θ (see equation (14)).

The butterfly diagram of the Sun (Figure 2) is used as a reference for this latitudinal dependence. The data are from the Greenwich USAF/NOAA observatory³ and provide the daily area of the spots, counted manually over the period 1874-2016. The panel (a) on Figure 2 shows the butterfly diagram with colours representing the area covered by the spots in unit of percent of visible hemisphere. It focuses on the observations after 1985 and covers two full solar cycles. Vertical colour bands highlight three time intervals : 1985-1989 (Purple), 1999-2002 (Blue) and 2006-2009 (Yellow). The two first are during a maximum of solar activity while the last one is for a minimum of activity. Due to the gradual migration of the spots over time, the longer observation period

³<https://solarscience.msfc.nasa.gov/greenwch.shtml>

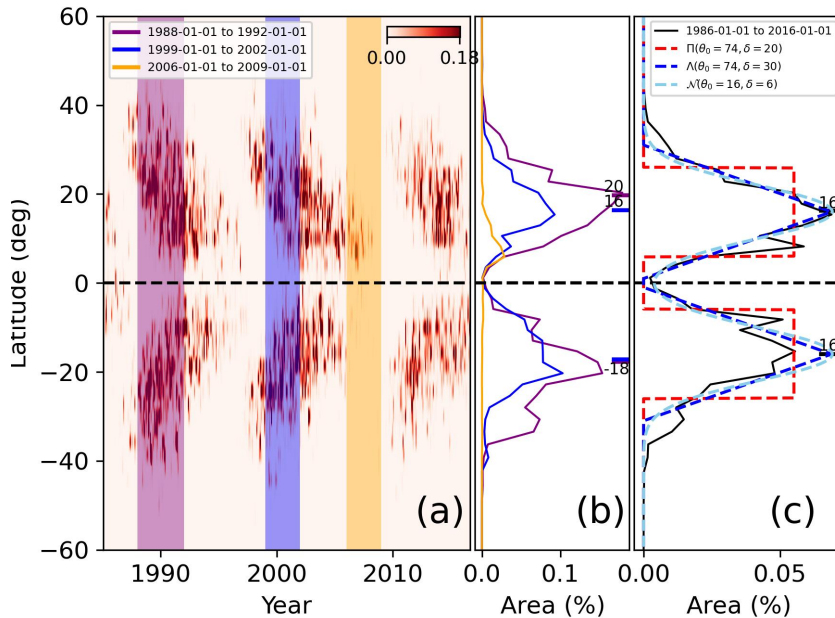


Fig. 2. Solar activity over time. (a) Butterfly diagram for the Sun. Vertical colour bands highlight periods of maximum of 1988-1992, 1999-2002 and minimum of activity of 2006-2009. (b) averaged spot area for the highlighted periods. Coloured ticks on (b) are the weighted mean for the activity latitude. (c) Filters $F(\theta|X)$ used for this study superimposed to solar data (1986-2016). Parameters θ_0 and δ are the latitude and the extension of the active region, respectively.

(1985-1989, 4 years) leads to a broader activity zone than the period 1999-2002. This indicates that 260
 the extension of the active region may not be trivial to measure in other stars because it will depend 261
 on the fraction of time the star is observed relative to the duration of its activity cycle. The activity 262
 cycles of Sun-like stars (if any) is a priori unknown, but Ca II H+K line emission and photometric 263
 studies (Oláh et al. 2009, 2016) suggest that it is of durations of roughly a few years to decades, as 264
 for the Sun. It indicates that over the course of several years, an active band as large as $\simeq 40^\circ$ may 265
 be expected. 266

Panel (b) of Figure 2 shows the cumulative area of spots as a function of the latitude and for the 267
 three considered periods. As noted earlier, the extension of the activity band is larger for the longest 268
 time-frame. The area of the spots during the active solar phase are symmetrical towards the equator. 269
 This suggests that when the activity is strong, $F(\theta|x)$ is almost north-south symmetric. This may be 270
 inaccurate for low activity phase, as shown for the period 2006-2009 but because $|Y_l^m(\theta, \phi)|^2$ is also 271
 symmetrical towards the equator, this has no incidence on the $a_j^{(AR)}(n, l)$ coefficients. 272

During the minimum, the total average area of the spots is a few times lower than during the 273
 maximum. It is also narrower, such as the integral in equation (14) is small, reducing $a_j^{(AR)}(n, l) \simeq 0$. 274
 During the phase of minimum of activity, the activity can effectively be considered as nonexistent 275
 (see Section 5 for the analysis on solar data), so that $a_2(n, l)$ is dominated by the centrifugal term 276
 $a_2^{(CF)}(n, l)$ and the other even a-coefficients are null. 277

The overall latitudinal profile is seemingly following a bell-shape with sharp slopes during 278
 periods of activity. Figure 2c compares data between 1986 and 2016 with three models for the 279

active latitudes: a model using the gate function $F(\theta|\mathbf{x}) = \Pi(\theta_0, \delta)$, a triangular function $\Lambda(\theta_0, \delta)$ and a Gaussian function $\mathcal{N}(\theta_0, \delta)$. The parameters of these were adjusted manually to approximately match the solar spot active latitudes profile. The triangular and the Gaussian functions describe equivalently the data, while the gate function initially proposed by Gizon (2002) is roughly fitting the data. Because spots are strictly appearing at latitudes below 45° , the Λ function may be the most suitable for the Sun. Nevertheless, these three functions are retained and compared here-further.

3.3. Assumptions on the a-coefficients

The most direct method for measuring the asphericity is to evaluate it directly for each mode (n,l) , that is, measuring the terms $a_j(n, l)$. This being already difficult for low-order a-coefficients of the Sun (Chaplin et al. 2003), it seems unreasonable to expect an accurate measurement of all individual $a_j(n, l)$ using asteroseismic data. These have a lower signal-to-noise ratio and severely reduced visibility at $l \geq 3$ due to the integrated photometry. After a trial and error process, jointly with power spectra simulations, we could identify a set of assumptions ensuring reliable and precise measurement of a-coefficients.

We first consider a fictitious star rotating as a solid-body with a solar activity level ($\epsilon_{nl} \simeq 5 \times 10^{-4}$, Gizon (2002)) with $a_1 = 1000$ nHz. The observed oscillation frequencies of 16 Cyg A are used here (Davies et al. 2015; Kamiaka et al. 2018). Split frequencies are derived using equations (1), (7), (13), (14), and converted into a-coefficients using equations (A.8-A.19). The a-coefficients are linear functions of the frequency, which is expected as $F(\theta|\theta_0, \delta)$ describes a single active region. Thus, a reasonable assumption is to consider those as pure first order polynomial functions of frequencies. However, tests on artificial spectra showed that it is often difficult to evaluate the slope of the a-coefficients. This is because the uncertainty on any a_j is at least of the same order as its variations within the range of observed frequencies. This suggests that current asteroseismic data lack the resolution and the signal-to-noise to reliably measure the frequency dependence on the a-coefficients.

Figure 3 shows $a_2^{(AR)}$, $a_4^{(AR)}$, $a_6^{(AR)}$ for activity described by $F = \Pi$ (black) or Λ (red) or \mathcal{N} (blue). These are the mean coefficients for the fictitious active star, as a function of θ_0 and δ . The figure indicates that there is a simple relationship between the a-coefficients, the co-latitude θ_0 and the extension of the activity zone δ , independently of the shape of activity. In the case of $F = \Pi$, the lines are cut near the pole and the equator due to the condition $\theta_0 \geq \delta/2$ and $\theta_0 \leq \pi - \delta/2$. In the other profiles, edges effects (truncation) has noticeable effects near the equator. The definition of δ differs between the three profiles, which explains that a factor of a few in $a_j^{(AR)}$ is noticeable between $F = \Pi$, Λ and \mathcal{N} for a given δ . Note that adding the centrifugal effect reduces $a_2(n, l) = a_2^{(AR)}(n, l) + a_2^{(CF)}(n, l)$, because the coefficient $a_2^{(CF)}(n, l)$ is always negative.

If an observation can constrain only a single a-coefficient (e.g. a_2), there often exists a degeneracy in θ_0 as multiple value of a_j can be obtained for a given θ_0 . As the figure shows, measuring two a-coefficients alleviates this degeneracy, provided that uncertainties are small enough. In other

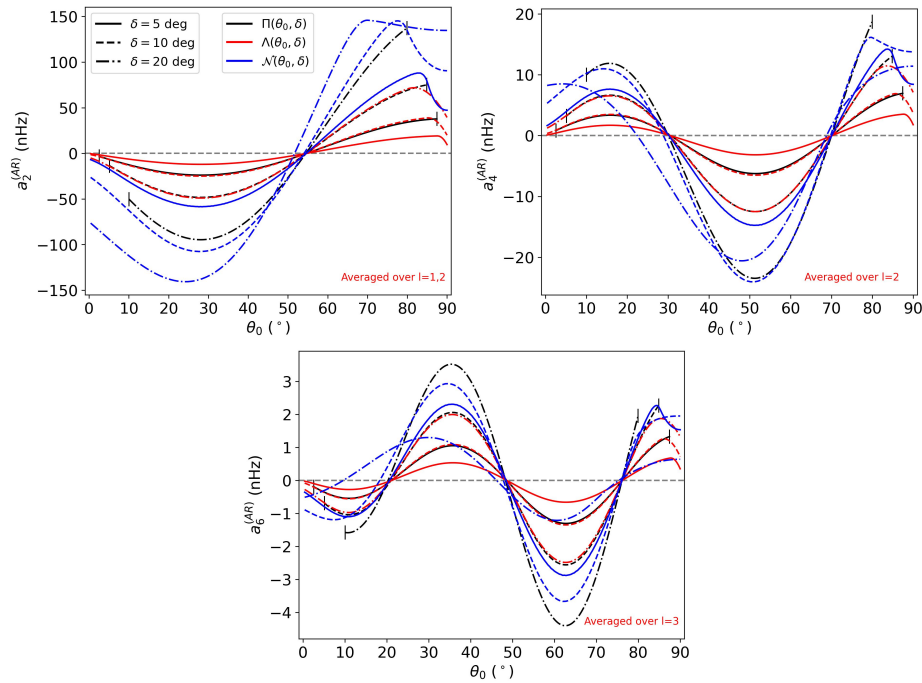


Fig. 3. Average $a_j^{(AR)}$ (no centrifugal effect accounted for) with $\epsilon_{nl} = 5.10^{-4}$ in function of θ and δ and for the gate (Π), triangle (Δ) and gaussian (Λ) filter functions. Uniqueness is guaranteed for θ only if at least two a-coefficients are measured.

words, the accuracy on the inference of the active region using a-coefficients is ensured only if we
317 can simultaneously constrain two a-coefficients (e.g. a_2 and a_4). This is essential to distinguish an
318 activity near the pole ($\theta_0 \lesssim 30^\circ$) from mid-latitude ($30^\circ \lesssim \theta_0 \lesssim 60^\circ$) or from near the equator
319 ($\theta_0 \gtrsim 60^\circ$).
320

It indicates that the loss of information resulting from the averaging does not affect the ac-
321 curacy⁴. Figure 3 also indicates that for a star with an activity intensity and an activity zone of
322 extension commensurate with the one of the Sun ($\epsilon_{nl} \simeq 5.10^{-4}$, $\delta \simeq 10^\circ$ when $F = \Pi$), the uncer-
323 tainty on $a_2^{(AR)}$ must be approximately $\lesssim 25$ nHz, the one for $a_4^{(AR)} \lesssim 10$ nHz and $a_6^{(AR)} \lesssim 1.5$ nHz to
324 be able to detect significant departures of the coefficients. This is to be compared with the spectral
325 resolution of 7-14nHz for 2-4 years of observation, typical of the longest Kepler observations. In
326 the Figure 3, $a_2^{(AR)}$ is obtained by averaging $l = 1, 2$, $a_4^{(AR)}$ by averaging $l = 2$, while $a_6^{(AR)}$ is only
327 constrained by $l = 3$ modes. Averaging $a_2^{(AR)}$ and $a_4^{(AR)}$ over $l = 1, 2, 3$ increases the maximum range
328 of the a-coefficients by a factor ≈ 1.5 for $a_2^{(AR)}$ and ≈ 2 for $a_4^{(AR)}$, respectively, without changing
329 the overall shape of the function. In Sun-like stars, the $l = 3$ modes have a HNR at least ten times
330 lower than $l = 0$ modes because the height ratio between $l = 3$ and $l = 0$ modes is around 0.08
331 for the Sun (Toutain & Gouttebroze 1993; Toutain et al. 1998). These modes are therefore difficult
332 to observe. Due to all of the above, it is extremely challenging to measure a_6 with current existing
333 data. In the following, we will thus focus on assessing the reliability domains of a_2 and a_4 only.
334

⁴It does however increase the uncertainty by a factor of a few.

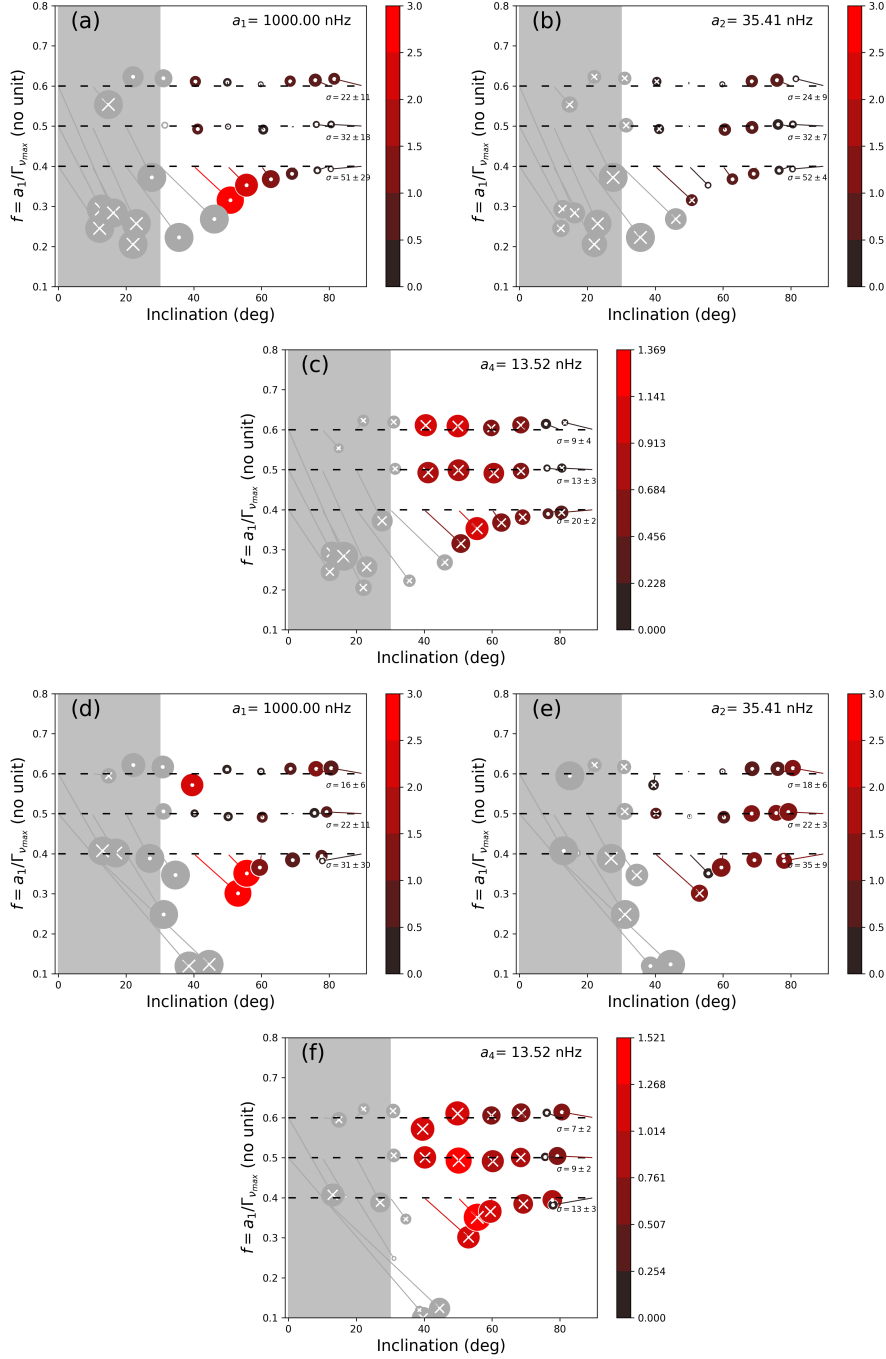


Fig. 4. Bias analysis for $\widehat{HNR} = 30$ for an equatorial activity band ($\theta_0 = 85^\circ, \delta = 10^\circ$) of similar intensity to the Sun ($\epsilon_{nl} = 5 \times 10^{-4}$), for $T_{obs} = 2$ years (top) and $T_{obs} = 4$ years (bottom). Colour and size of the circles indicate the modulus of the bias. The colour bar gives its scale normalised by the uncertainty, $b(a_j)/\sigma$. A white cross is for an underestimation. A white dot is for an overestimation. Below 30° of inclination (gray area and symbols), the results are not reliable.

335 4. Bias analysis on a_1 a_2 and a_4

336 In order to understand the reliability of the inference on low-degree a-coefficient, it is necessary to
 337 perform a bias analysis. This requires to fit an ensemble of emulated spectra that are representative
 338 of Sun-like stars and to compare the results with the true inputs.

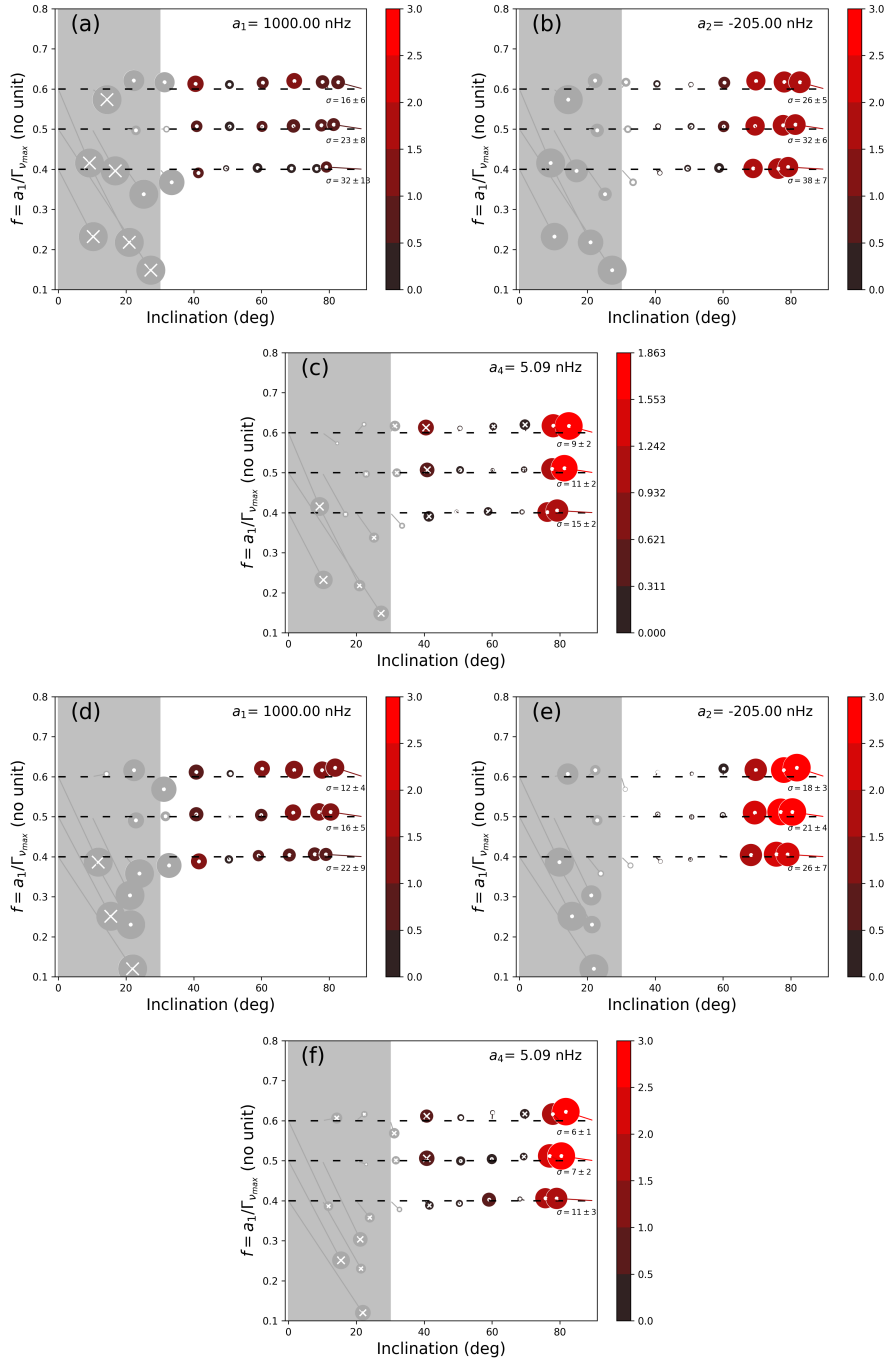


Fig. 5. Bias analysis for $\widehat{HNR} = 30$ for a large polar activity cap ($\theta_0 = 22.5, \delta = 45$) of similar intensity to the Sun ($\epsilon_{nl} = 5.10^{-4}$), for $T_{obs} = 2$ years (top) and $T_{obs} = 4$ years (bottom).

4.1. Test setup

339

The synthetic spectra use the frequencies, heights, widths and the noise background profile of 16 Cyg A as a template for the simulations. We want to specifically study the impact of the mode blending (effect of $a_1/\Gamma_{v_{max}}$), the stellar inclination (i), observation duration (T_{obs}) and of the maximum Height-to-Noise background (\widehat{HNR}) on the accuracy of a_1 , a_2 and a_4 . Grids of spectra are built in the case of an equatorial band of activity and of a large polar activity. The grid parameters and their ranges are provided in Table 4.1 and discussed further below. The spectra are made using

340

341

342

343

344

345

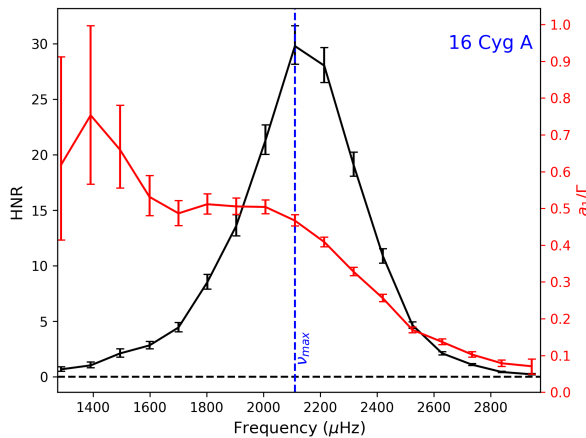


Fig. 6. HNR (black) and a_1/Γ ratio (red) for 16 Cyg A, which is the reference star used to make simulations.

346 a spectrum simulator code⁵ that take the reference star (or template) and modify its properties to
 347 match the requirement of the user. The template is altered in terms of HNR following a similar
 348 approach as in Kamiaka et al. (2018). The main difference is that we considered a frequency-
 349 dependent noise background. Heights are rescaled according to,

$$H_{n,l=0} = \frac{\widehat{HNR}}{\widehat{HNR}_{\text{ref}}} H_{\text{ref}}(n, l=0) \quad (17)$$

350 where \widehat{HNR} is the maximum HNR of the synthetic star, $\widehat{HNR}_{\text{ref}}$ the maximum HNR of the reference
 351 star and $H_{\text{ref}}(n, l=0)$ the $l=0$ heights of the reference star.

352 As for the mode blending factor $f = a_1/\Gamma_{\nu_{\text{max}}}$, it is calculated fixing a_1 and altering $\Gamma_{\nu_{\text{max}}}$ such
 353 that,

$$\Gamma_{\nu_{\text{max}}} = \frac{a_1}{f}. \quad (18)$$

354 A fiducial value of $a_1 = 1000$ nHz ($\simeq 2.4$ the solar rotation) is used in the simulation. Note that this
 355 differs from Kamiaka et al. (2018) where the splitting was modified in order to obtain the desired
 356 mode blending factor.

357 As shown in Table 4.1, three HNR cases are investigated, ranging from 10 to 30. Two ob-
 358 servation durations are considered: 2 years and 4 years. This is representative of the best Kepler
 359 observations (Davies et al. 2015) and of future observations from PLATO (Rauer et al. 2014).
 360 Similarly to the test cases of Gizon (2002), a_2 and a_4 are determined for an equatorial activity of
 361 extension of the same order as in the Solar case ($\delta \simeq 10^\circ$), and in the case of a large polar cap
 362 ($\delta = 45^\circ$). Both situations assume an activity of the same order as for the Sun. The priors are set
 363 in a similar manner as they would if the power spectrum was from a real star. The evaluation of
 364 the mode parameters is performed using a MCMC method, like for actual stars (see Appendix B
 365 for further details), but on the limit-spectrum (no noise). Fitting the limit spectrum allows to assess

⁵The tool suite used here along with the data inputs/outputs are available at https://github.com/OthmanB/Benomar2022/tree/version_2.

Table 1. Parameters set to construct artificial power spectra. a_2 and a_4 are determined assuming active regions located either in an equatorial band or in a polar cap.

| Variable | Values | |
|--------------------------|--|---|
| HNR | 10, 20, 30 | |
| T_{obs} (years) | 2, 4 | |
| $a_1/\Gamma_{v_{\max}}$ | 0.4, 0.5, 0.6 | |
| ϵ_{nl} | $5 \cdot 10^{-4}$ | |
| a_1 (nHz) | 1000 | |
| Act. Region | $\theta_0 = 85^\circ, \delta = 10^\circ$ (Eq.) | $\theta_0 = 22.5^\circ, \delta = 45^\circ$ (Pol.) |
| a_2 (nHz) | 35.41 | -205.06 |
| a_4 (nHz) | 13.52 | 5.09 |

Table 2. Summary of the main parameters for the Sun and 16 Cyg A and B used to infer the activity. fiducial biases $b(a_2)$ and $b(a_4)$ for 16 Cyg A and B are set after inspection of Figure 4. The lowest (highest) solution of a_4 for 16 Cyg B is has a probability of 30% (70%).

| | Active Sun | Quiet Sun | 16 Cyg A | 16 Cyg B |
|---------------------------|-----------------|-----------------|-----------------|-----------------------------------|
| \widehat{HNR} | 100 | 70 | 30 | 29 |
| $\Delta\nu$ (μ Hz) | 135.1 | 135.1 | 103.35 | 116.92 |
| a_1 (nHz) | 421 ± 10 | 410 ± 9 | 614 ± 37 | 607 ± 78 |
| a_1/Γ | 0.45 ± 0.03 | 0.40 ± 0.02 | 0.45 ± 0.04 | 0.58 ± 0.1 |
| inclination ($^\circ$) | 90 (fixed) | 90 (fixed) | 45 ± 4 | 35 ± 3 |
| a_2 (nHz) | 80 ± 19 | 11 ± 21 | 19.6 ± 8.6 | 18.5 ± 23.5 |
| a_4 (nHz) | 5.0 ± 10.5 | 2.1 ± 9.8 | 2.9 ± 8.9 | -27.9 ± 6.5 or -1.0 ± 6.7 |
| $a_2^{(\text{CF})}$ (nHz) | -6.5 ± 0.3 | -6.1 ± 0.3 | -17.0 ± 2.2 | -15.5 ± 4.0 |
| $a_2^{(\text{AR})}$ (nHz) | 86.2 ± 18.7 | 16.7 ± 20.4 | 39.0 ± 20.6 | 34.0 ± 21.8 |
| $b(a_2)$ (nHz) | / | / | -10 | -10 |
| $b(a_4)$ (nHz) | / | / | -10 | -10 |

the systematic errors by calculating the expectation value of the probability density function. The 366
expected uncertainty can also be known by computing the standard deviation. 367

4.2. Results

 368

To appreciate the level of inaccuracy achieved when measuring a_j , $j \in [1, 2, 4]$ coefficients, the bias 369
is calculated for a_j , $f = a_1/\Gamma_{v_{\max}}$ and i , 370

$$\begin{aligned} b(a_j) &= E[a_j^{\text{meas}}] - a_j^{\text{true}}, \\ b(F) &= E[F^{\text{meas}}] - F^{\text{true}}, \\ b(i) &= E[i^{\text{meas}}] - i^{\text{true}}. \end{aligned} \quad (19)$$

Here, the letter E refers to the expectation value (median) from the probability density function. 371

Figure 4 shows the resulting bias maps for a-coefficients as a function of the blending factor F 372
and of the stellar inclination for a-coefficients corresponding to an equatorial activity band. Figure 5 373
is the same but for a large polar activity cap. The bias is represented as a projected three dimensional 374
vector using the three quantities defined by equation (19) and for $j \in [1, 2, 4]$. To evaluate the 375
importance of the bias on a_j , the plot shows $b(a_j)/\langle \sigma_{a_j}(i, F) \rangle_i$, with $\langle \sigma_{a_j}(i, F) \rangle_i$ the average standard 376
deviation of the probability density functions obtained by the MCMC sampling over $i \in [30^\circ, 90^\circ]$. 377
The value of $\langle \sigma_{a_j}(i, F) \rangle_i$ (noted σ for convenience hereafter) and its variance along the inclination 378

379 axis is also shown on the plots. A value of $b(a_j)/\sigma$ greater than one indicates that the inaccuracy
 380 exceeds the typical expected uncertainty at 1σ and may lead to significantly biased results during
 381 the subsequent analyses of the a-coefficients. A negative bias (underestimation) for a_j is indicated
 382 by a cross within the circle while a positive bias (overestimation) by a dot. The darker the colour,
 383 the smaller the norm of the normalised bias. The size of the circle symbols is also proportional to
 384 the bias, but capped to 3, to avoid excessively large symbols when $i < 30^\circ$ (see next paragraph for
 385 explanations). The case of observations of duration of 2 years are in the top figures (a, b, c) while
 386 the 4 years observation case is shown in bottom figures (d, e, f).

387 We first note that the biases on inclination and on F are consistent with results from Kamiaka
 388 et al. (2018). Regions of stellar inclination below 30° are found to provide very unreliable results
 389 and the median of the inclination is biased toward $\simeq 80^\circ$ when the true input is $i = 90^\circ$. Meanwhile,
 390 biases in a_1 are found to often exceed 50% in the gray area⁶, indicating that for inclination below
 391 $\simeq 30^\circ$, the median estimator of the probability density function might not be trusted. This justifies
 392 also the range for the calculation of σ . In the following we therefore focus the discussion of the
 393 figures for the region above 30° .

394 In the case of an equatorial zone of activity, we note that measurements of a_1 may have negligi-
 395 ble inaccuracies when the blending factor F is above 0.4, but starts to be significantly deteriorated
 396 at (and probably below) $f = 0.4$ because $|b(a_1)|/\sigma$ exceeds 1.5 when $i < 50^\circ$. Split components
 397 are then overlapping significantly leading to important degeneracies between a-coefficients, mode
 398 widths and the stellar inclination. Meanwhile, we note that the biases on a_2 and a_4 remain mild
 399 compared to the uncertainty ($|b(a_2)|/\sigma < 1$ and $|b(a_4)|/\sigma < 1$), even for $f = 0.4$.

400 In the case of a polar active region, $|a_2|$ represents $\simeq 20\%$ of the a_1 coefficient. In these condi-
 401 tions, we note that $b(a_1)/\sigma$ does not exceed the unity (see (a) and (d)), indicating a good accuracy.
 402 The terms $|b(a_2)|/\sigma$ and $|b(a_4)|/\sigma$ are also lower than 0.5, provided that the stellar inclination is
 403 between 30° and 70° . This indicates that a large a_2 coefficient is generally associated with a higher
 404 accuracy for all a-coefficients. The plot also demonstrates that a large zone in the parameter space
 405 has moderate to small bias.

406 Interestingly, figures for \widehat{HNR} of 10 and 20 (Figures D.1-D.4 in Appendix D) lead to similar
 407 conclusions. Therefore, even in less favourable \widehat{HNR} conditions, the expected uncertainty on the
 408 measurement generally encompass the bias provided that the stellar inclination exceeds $\simeq 30^\circ$
 409 (ensuring that $m \neq 0$ have significant amplitudes) and that the mode blending factor is above 0.4.
 410 This indicates that for a majority of stars observed by Kepler, the accuracy may not be a major issue
 411 when measuring a_1 , a_2 and a_4 and provided that a careful assessment of F and i is performed. Note
 412 however that the average uncertainty σ does usually increase when the \widehat{HNR} and/or the observation
 413 duration decrease, which will have an impact on the precision of the determination of the active
 414 region.

⁶This is likely due to the fit mis-identifying the $l = 2, m = \pm 1$ with $l = 2, m = \pm 2$, effectively doubling or halving the a_1 coefficient.

Table 3. Statistical summary for the activity parameters and their model log-marginal likelihood $\ln(P(\mathbf{O}|\mathbf{M}_{\text{AR}}))$ when $F(\theta|\mathbf{x}) = \Pi(\theta_0, \delta)$, $\Lambda(\theta_0, \delta)$ or $\mathcal{N}(\theta_0, \delta)$. $\ln(P(\mathbf{O}|\mathbf{M}_{\text{CF}}))$ is the log-marginal likelihood for a pure centrifugal effect. The Activity significance is the probability that the activity is necessary to explain the data and derived from the log-marginal likelihoods. Uncertainty on the activity significance is less than 0.25%.

| | Active Sun | Quiet Sun | 16 Cyg A | | 16 Cyg B | | bias corr. |
|---|---------------------------|-----------------------|------------------------|------------------------|-----------------------|------------------------|------------------------|
| | . | . | No bias | bias corr. | No bias | $a_4 \approx -27.9$ | $a_4 \approx -1.0$ |
| $\ln(P(\mathbf{O} \mathbf{M}_{\text{CF}}))$ | -10.809 | -0.367 | -1.856 | -3.889 | -10.596 | -1.228 | -5.910 |
| $\Pi(\theta_0, \delta)$ | $\epsilon_{nl} (10^{-4})$ | $7.6^{+25.5}_{-5.3}$ | $3.7^{+19.6}_{-3.1}$ | $5.3^{+19.6}_{-4.1}$ | $6.4^{+24.8}_{-4.8}$ | $12.5^{+31.9}_{-7.5}$ | $4.6^{+20.8}_{-3.7}$ |
| | θ_0 (deg) | 76^{+8}_{-7} | 60^{+19}_{-41} | 71^{+13}_{-14} | 79^{+8}_{-10} | 58^{+3}_{-3} | 67^{+14}_{-25} |
| | δ (deg) | 7^{+16}_{-5} | 2^{+11}_{-2} | 4^{+16}_{-3} | 5^{+15}_{-4} | 8^{+17}_{-6} | 3^{+13}_{-2} |
| $\ln(P(\mathbf{O} \mathbf{M}_{\text{AR}}))$ | -0.685 | -0.347 | -0.482 | -0.656 | -0.878 | -0.449 | -0.781 |
| Significance (%) | > 99.99 | 50.5 | 79.8 | 96.2 | > 99.9 | 68.6 | 99.3 |
| $\Lambda(\theta_0, \delta)$ | $\epsilon_{nl} (10^{-4})$ | $14.2^{+33.0}_{-9.8}$ | $17^{+42.9}_{-14.2}$ | $15.4^{+39.5}_{-12.2}$ | $13.6^{+34.1}_{-4.8}$ | $21.1^{+35.2}_{-12.6}$ | $15.1^{+38.9}_{-12.4}$ |
| | θ_0 (deg) | 76^{+9}_{-8} | 49^{+27}_{-27} | 66^{+16}_{-41} | 78^{+9}_{-21} | 58^{+2}_{-3} | 58^{+21}_{-40} |
| | δ (deg) | 7^{+16}_{-5} | 6^{+19}_{-5} | 6^{+17}_{-4} | 5^{+15}_{-4} | 10^{+16}_{-6} | 6^{+17}_{-5} |
| $\ln(P(\mathbf{O} \mathbf{M}_{\text{AR}}))$ | -0.698 | -0.296 | -0.492 | -0.699 | -0.930 | -0.427 | -0.847 |
| Significance (%) | > 99.99 | 51.8 | 79.6 | 96.0 | > 99.99 | 69.0 | 99.4 |
| $\mathcal{N}(\theta_0, \delta)$ | $\epsilon_{nl} (10^{-4})$ | $3.7^{+16.0}_{-2.0}$ | $15.1^{+42.8}_{-13.5}$ | $12.2^{+39.5}_{-10.5}$ | $6.6^{+24.3}_{-5.0}$ | $13.3^{+24.1}_{-7.0}$ | $12.6^{+41.0}_{-11.0}$ |
| | θ_0 (deg) | 73^{+11}_{-10} | 48^{+28}_{-34} | 63^{+18}_{-38} | 75^{+11}_{-27} | 56.6^{+3}_{-7} | 55^{+23}_{-37} |
| | δ (deg) | $9^{+26.6}_{-8}$ | 7^{+20}_{-6} | 6^{+22}_{-5} | 4^{+20}_{-3} | 6^{+22}_{-5} | 7^{+21}_{-6} |
| $\ln(P(\mathbf{O} \mathbf{M}_{\text{AR}}))$ | -0.708 | -0.384 | -0.584 | -0.811 | -0.943 | -0.516 | -0.811 |
| Significance (%) | > 99.99 | 49.6 | 78.1 | 95.6 | > 99.99 | 67.1 | 99.4 |
| Average | $\epsilon_{nl} (10^{-4})$ | $7.7^{+25.7}_{-5.6}$ | $11.4^{+41.6}_{-10.0}$ | $9.2^{+34.2}_{-7.5}$ | $8.0^{+29.4}_{-6}$ | $15.5^{+30.7}_{-9.1}$ | $10.5^{+37.2}_{-9.0}$ |
| | θ_0 (deg) | 75^{+10}_{-8} | 53^{+25}_{-37} | 68^{+14}_{-36} | 78^{+9}_{-14} | 58^{+3}_{-4} | 61^{+18}_{-34} |
| | δ (deg) | 7^{+22}_{-6} | 5^{+18}_{-4} | 5^{+18}_{-4} | 5^{+17}_{-4} | 8^{+18}_{-6} | 6^{+18}_{-5} |
| $\ln(P(\mathbf{O} \mathbf{M}_{\text{AR}}))$ | -0.697 | -0.342 | -0.519 | -0.722 | -0.917 | -0.464 | -0.824 |
| Significance (%) | > 99.99 | 50.6 | 79.2 | 96.0 | > 99.99 | 68.2 | 99.4 |
| | | | | | | | 90.7 |

5. Analysis of solar data

415

The Sun has a well-known 11-year activity cycle that makes it ideal for testing further the accuracy of the method. The Sun activity cycle is analysed at two instants, highlighted in Figure 2 and for which high-quality helioseismic data are available: (a) the maximum of activity between January 1999 and January 2002; and (b) the minimum of activity between January 2006 and January 2009. Data are from the Variability of Solar Irradiance and Gravity Oscillations instrument aboard SOHO spacecraft (Frohlich et al. 1997) and presents very few gaps.

416

417

418

419

420

421

5.1. a-coefficients of the Sun

422

As for the simulated data, the analysis consists in fitting the power spectrum for cases (a) and (b), to measure the a_1 , a_2 and a_4 coefficients using the Bayesian modelling and the MCMC method described in the Appendix B. Figures of the best fits and their discussions are provided in Appendix E. The goal being to evaluate the accuracy of the inference of the activity zone from a-coefficients, the presented results are for a stellar inclination fixed to 90° , instead of having it as a free parameter. This value correspond approximately to the stellar inclination as seen by the SOHO satellite. This

423

424

425

426

427

428

429 alleviates biases on a_j coefficients that may arise due to the systematic underestimation of i when
 430 it is close to 90 degrees. However, carried tests with a free inclination during the maximum of
 431 activity⁷ lead to a difference of -12nHz in a_2 and to -1.3nHz in a_4 . This is consistent with the
 432 expected difference from the bias map of Figure 4. In agreement with the discussion of Section 4,
 433 the difference does not have a significant impact on the activity inference because the uncertainties
 434 for those parameters are larger than the observed measurement shift.

435 Figure 7 shows the measured probability distribution function of the relevant parameters along
 436 with their correlations during the maximum of solar activity (left) and the minimum (right). The
 437 $a_2^{(CF)}$ distribution in red represents the expected centrifugal effect on a_2 as derived from frequency
 438 shifts $\delta_{nlm}^{(CF)}$ of equation (13). The distributions are Gaussians and show a weak correlation, reflecting
 439 the quality of the data. Between the maximum and the minimum of activity, the a_2 coefficient
 440 drifted significantly, from $a_2 = 80 \pm 19 \text{nHz}$ to $a_2 = 11 \pm 21$ falling within the 1σ confidence
 441 interval of the centrifugal term. Although a_4 may have changed, the effect is below uncertainty
 442 levels and remain close to 0. As shown in Figure 15, other time intervals may lead to a_4 departing
 443 from 0. The figures demonstrate that a comparison of a_2 and $a_2^{(CF)}$ may reveal the activity of a Sun-
 444 like star. At the maximum of activity $a_2^{(CF)}$ is inconsistent with a_2 at 4.5σ , but it is in agreement at
 445 1σ during the minimum of activity. Interestingly, Chaplin et al. (2003) also studied in details the
 446 frequency asymmetry of $l = 2$ modes using BiSON and GOLF data with a different methodology,
 447 and over period that encompasses the maximum of 1999-2002. Their measure consider only T_{n22}
 448 so a direct comparison is not straightforward. However, we note that with a 844 day-long timeseries
 449 starting in Feb 1999⁸, they detect a frequency shift $T_{n22} \simeq 190 \text{nHz}$ at a similar significance ($\simeq 4\sigma$)
 450 than us when averaging over all modes between $\simeq 2000 - 3300 \mu\text{Hz}$ (to be compared to our range
 451 of $\simeq 2300 - 3600 \mu\text{Hz}$). Their Figure 8 also show that the global effect of the activity cycle between
 452 1994 and 2000 is evident on the averaged T_{n22} while the frequency dependence of T_{n22} may have
 453 too large uncertainties to ascertain a frequency-trend. This is in line with our own findings (see our
 454 Section 3.3).

455 A rigorous statistical evaluation of our significance requires the joint use of a_2 and a_4 . This is
 456 discussed in Section 5.2, along with other activity results. Finally note that for inclination of $\simeq 90$
 457 degrees, it is not possible to determine a_3 , because the amplitudes of the azimuthal components for
 458 $l = 1, 2$, are not favourable (Gizon & Solanki 2004).

459 5.2. Activity of the Sun

460 The activity intensity and its latitudinal coverage is derived from a fit of the $a_2^{(AR)}$ and $a_4^{(AR)}$ coef-
 461 ficients. Technical details are in Appendix C. Statistical summary of the results are listed in Table
 462 3. The statistical significance of the activity exceeds 99.99% (highly significant) at the maximum
 463 of activity, but is around 50.6% (not significant) during the minimum of activity, demonstrating
 464 the possibility of detecting activity in Sun-like stars. The choice of the function F describing the

⁷The measured stellar inclination is $i = 74 \pm 3$ degrees at the maximum of activity of 1999-2002.

⁸To be compared to our timeseries of 1095 days starting in Jan 1999.

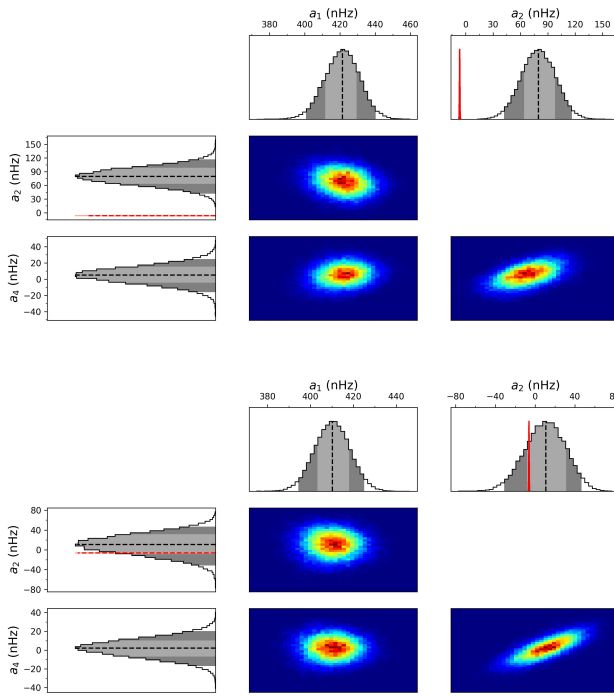


Fig. 7. Probability Density Functions and their correlations, obtained by MCMC for coefficients a_1, a_2, a_3, a_4 for the Sun at Maximum of activity (1999-2002, left) and at minimum of activity (2006-2009, right). The red curve is the expected a_2^{CF} coefficient for a pure centrifugal distortion. The light and dark gray PDF filling is for the 1σ and 2σ confidence interval, respectively.

active region changes the detection significance by only a few percents. The three explored models 465 fit equivalently the data implying that the shape of the active region cannot be determined with 466 currently available a_2 and a_4 constraints. 467

Figure 8 and 9 show $\epsilon_{nl} = \epsilon, \theta_0$ and δ for the Sun at its maximum of activity (1999-2002) and 468 its minimum (2006-2009), respectively. There is no major differences between the three activity 469 profiles, although it is noted that uncertainties are larger in the case of a triangular and a Gaussian 470 activity zone. During the maximum of activity, $\epsilon \simeq 0$ is clearly excluded (see inset). With $F = \Pi$, 471 we observe a log-normal distribution, with median $7.6 \cdot 10^{-4}$, consistent with the value reported by 472 Gizon (2002). However, the uncertainty is large, suggesting that only the order of magnitude can 473 be constrained in Sun-like stars. At the minimum of activity, the log-normal distribution morphs 474 into a $1/x$ law, similar to the Jeffreys prior. This is a sign of weaker statistical significance for the 475 activity. 476

The co-latitude $\theta_0 \simeq 75^\circ$ is consistent with the butterfly diagram, which suggests $\theta_0 \simeq 80^\circ$. At 477 the minimum of activity and despite a non-significant detection, the probability distribution of θ_0 478 shows a weak indication of activity at mid and high co-latitudes. Despite the high significance of 479 the detection during the maximum of activity, δ is poorly constrained, showing that this parameter 480 is challenging to measure on the Sun and on other Sun-like stars. 481

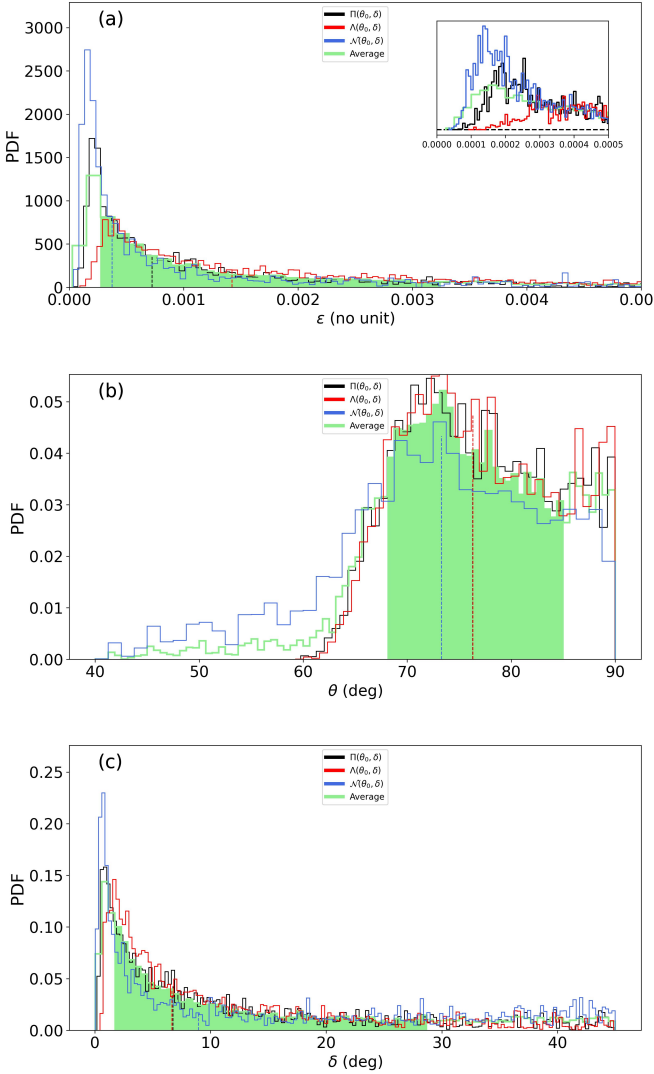


Fig. 8. Inferred pdf for (a) ϵ , (b) θ_0 and (c) δ , during the Sun maximum activity of 1999-2002. The inset of (a) is a zoom into the near-zero ϵ values with smaller binning.

482 6. Analysis of 16 Cyg A and B

483 Due to their brightness (magnitudes $V=5.95$ and 6.20) 16 Cyg A and B have modes with the highest
 484 HNR among all of Sun-like stars observed asteroseismically so far. They constitute ideal candidates
 485 to evaluate the activity. The two stars are wide binaries, with a confirmed planet around 16 Cyg B
 486 (Cochran et al. 1997) and were extensively studied (e.g. Neckel 1986; King et al. 1997; Deliyannis
 487 et al. 2000; Schuler et al. 2011; Takeda 2005; Metcalfe et al. 2012; Lund et al. 2014; Verma et al.
 488 2014; Buldgen et al. 2015; Deal et al. 2015; Metcalfe et al. 2016; Roxburgh 2017; Bellinger et al.
 489 2017; Maia et al. 2019; Bazot et al. 2019; Bazot 2020; Farnir et al. 2020; Morel et al. 2021; Buldgen
 490 et al. 2022; Nsamba et al. 2022). The 2.5 years (13 September 2010 to 8 March 2013) observation
 491 by the Kepler space-borne instrument is used in this section to measure pulsation parameters. The
 492 data are the same as those used in Bazot et al. (2019) for which instrumental issues (outliers, jumps,
 493 trends) and the quarter stitching is performed using the procedure described in García et al. (2011a).
 494 The binary system has precisely measured angular diameters, making it two of the few Sun-like

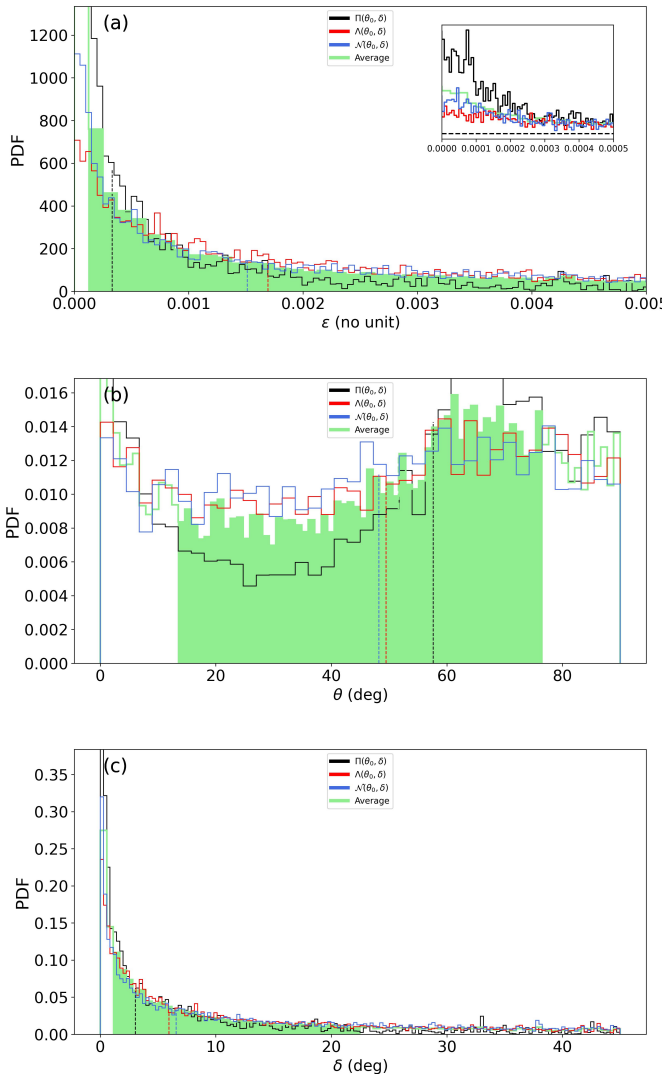


Fig. 9. Inferred pdf for (a) ϵ , (b) θ_0 and (c) δ , during the Sun minimum activity of 2006-2009. The inset of (a) is a zoom into the near-zero ϵ values with smaller binning.

stars with known interferometric radii. Their measured radius are $1.22 \pm 0.02R$ and $1.12 \pm 0.02R$ for 495
16 Cyg A and B, respectively (White et al. 2013). Their spectroscopic parameters are very close to 496
those of the Sun: Their effective temperatures are $T_{\text{eff}} = 5825 \pm 50$ K, $T_{\text{eff}} = 5750 \pm 50$ K and their 497
metallicity are $[M/H] = 0.10 \pm 0.09$, $[M/H] = 0.05 \pm 0.06$ (Ramírez et al. 2009) for 16 Cyg A and 498
B, respectively. With an estimated age of around 7 Gyrs for both stars (Metcalfe et al. 2016; Bazot 499
2020, e.g.), they are significantly older than the Sun. 500

6.1. Seismic constraints for 16 Cyg A

Earlier studies of 16 Cyg A revealed around 60 modes of pulsations with significance in the power 502
spectrum⁹. The asteroseismic analysis of Davies et al. (2015) found a stellar inclination of 56^{+6}_{-5} 503
and a rotation $23.8^{+1.5}_{-1.8}$ ($\langle \delta\nu_{nlm}/m \rangle_{nl} \simeq 486^{+40}_{-29}$ nHz). Using a refined power spectrum modelling that 504

⁹The exact value may differ from author to author, due to different choice for the significance.

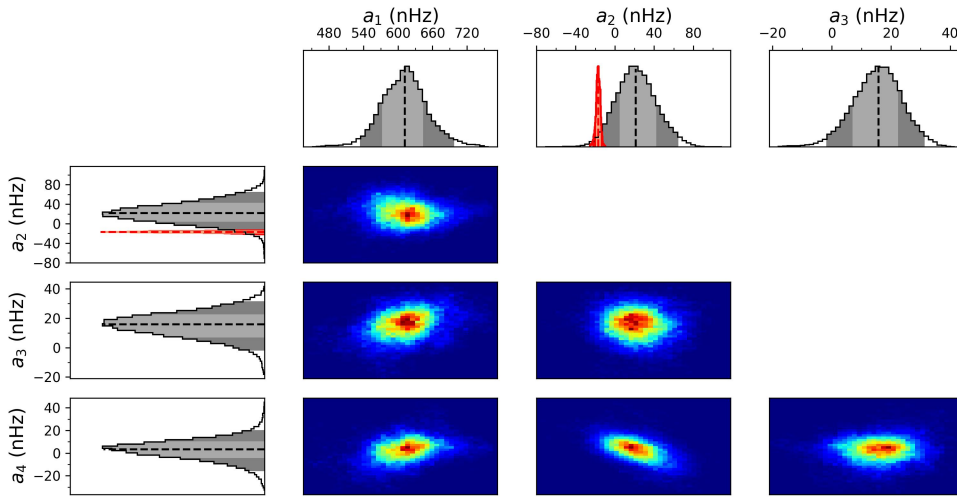


Fig. 10. Probability Density Functions and their correlations, obtained by MCMC of the power spectrum of 16 Cyg A and for coefficients a_1, a_2, a_3, a_4 for 16 Cyg A. The red curve shows the expected a_2^{CF} coefficient for a pure centrifugal distortion of the star. The light and dark gray PDF filling is for the 1σ and 2σ confidence interval, respectively.

505 account for a_1, a_3 and parameterises the cavity asphericity $(R_{\text{eq}} - R_{\text{pol}})/R_{\text{eq}}$, Bazot et al. (2019)
 506 reported values ($i = 58.5 \pm 6.8, a_1 = 464 \pm 43\text{nHz}$), consistent with Davies et al. (2015).

507 Figure 10 shows the probability density function for a_1, a_2, a_3 and a_4 for 16 Cyg A, along
 508 with their correlation and with $a_2^{(CF)}$ superimposed in the a_2 quadrant. Table 2 synthesises the in-
 509 ferred values of the coefficients. The probability density functions are near-Gaussian and thus the
 510 quadratic mean of the asymmetrical uncertainties is reported in the table. The a_1 coefficient is sig-
 511 nificantly lower than past estimates but remain consistent at a 2σ confidence level. The difference
 512 may be due to the lower stellar inclination $i = 45 \pm 4$, that is also only consistent with earlier de-
 513 termination at 2σ . The a_3 coefficient is marginally greater but with smaller uncertainty than Bazot
 514 et al. (2019) (they reported $a_3 = 11.15 \pm 10.95\text{nHz}$).

515 More importantly, a_2 is positive at 1σ , which is consistent with the assertion of star prolateness
 516 from Bazot et al. (2019) and is inconsistent with the centrifugal distortion term, $a_2^{(CF)}$. Finally, a_4 ,
 517 includes zero within 1σ .

518 With respect to Figures 4-5, $a_1/\Gamma_{\nu_{\text{max}}} = 0.45 \pm 0.04$ and $i = 45 \pm 4^\circ$ place 16 Cyg A in a
 519 parameter space where the expected magnitude of the bias for a_1, a_2 and a_4 is of the order of 0.5σ ,
 520 0.5σ and 0.8σ respectively. This remains accurate even when accounting for the slightly higher
 521 estimates of inclination from previous publications. Translated into absolute units, this corresponds
 522 to approximately $b(a_1) \simeq +10\text{nHz}$ (overestimation), $b(a_2) \simeq -10\text{nHz}$ (underestimation), $b(a_4) \simeq$
 523 -10nHz (underestimation). These fiducial values are used in Section 6.3 to evaluate the effect of
 524 the potential bias on the estimates of the activity zone.

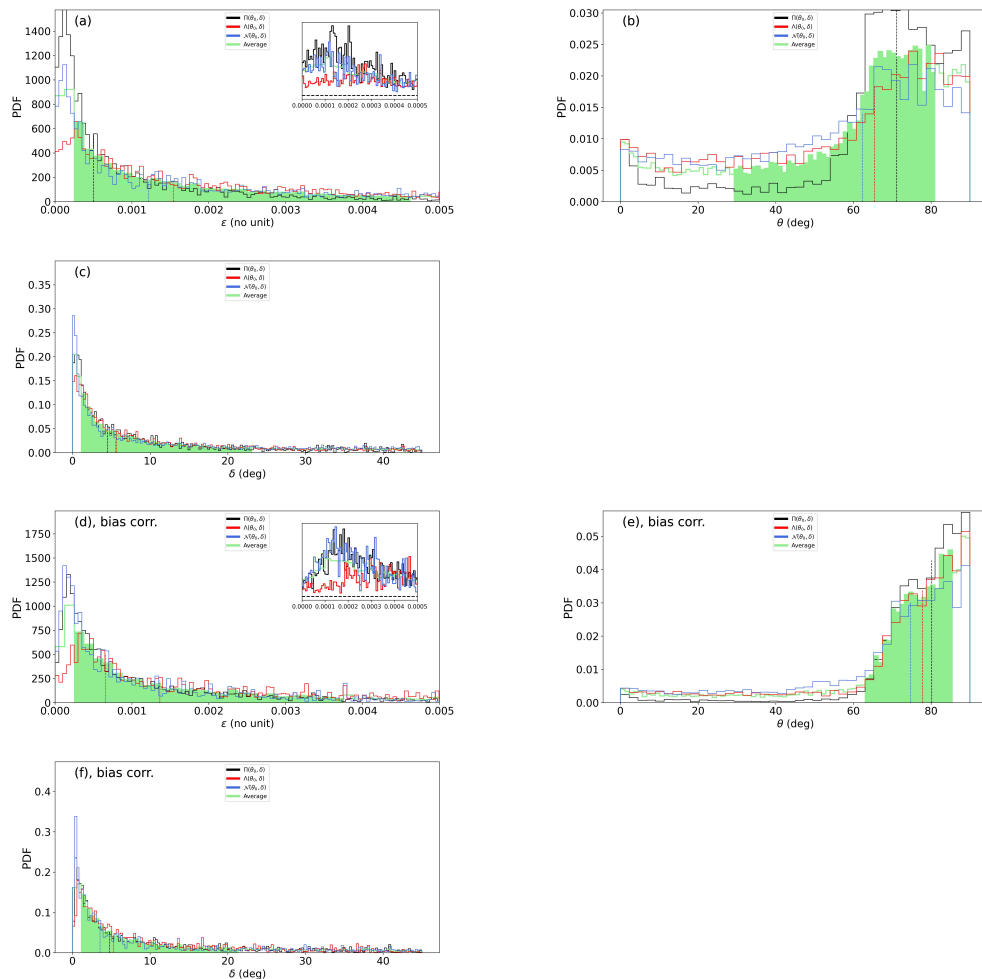


Fig. 11. Inferred pdf for 16 Cyg A for raw measures (a,b,c) or with bias correction (d,e,f). The green curve is for the average pdf with $F = \Pi$, Λ and \mathcal{N} . The shaded area is its 1σ confidence interval. The inset of (a) and (d) is a zoom into the near-zero ϵ values with smaller binning.

6.2. Seismic constraints for 16 Cyg B

525

Similarly to 16 Cyg A, 16 Cyg B has around 60 observed modes. However, the reported precision for the past determination of the seismic parameters is less accurate than for 16 Cyg A, despite a similar HNR. Davies et al. (2015) and Bazot et al. (2019) both note a large degeneracy between the stellar inclination and the average rotation rate, with even a clear bi-modality in the distributions obtained by Bazot et al. (2019). Their global solution of $i = 36^{+17}_{-7}$ is associated with two separate solutions for a_1 , centred around $\simeq 300$ nHz and $\simeq 550$ nHz, that they use to infer the latitudinal differential rotation profile. Meanwhile, as for 16 Cyg A, the star is found to be prolate, indicating a surface activity.

Figure 12 shows the measured a-coefficients. It appears that including the a_4 coefficient remove the degeneracy issue observed by previous publications. The stellar inclination, a_1 and a_2 are precisely determined and have approximately Gaussian probability distributions and these are reported as such in Table 2. The found rotation rate a_1 correspond to the higher solution of rotational splitting of Davies et al. (2015) and Bazot et al. (2019) (see their Figures of probability density functions). Meanwhile, the degeneracy observed in a_1 in earlier studies is moved to a_4 : It exhibits

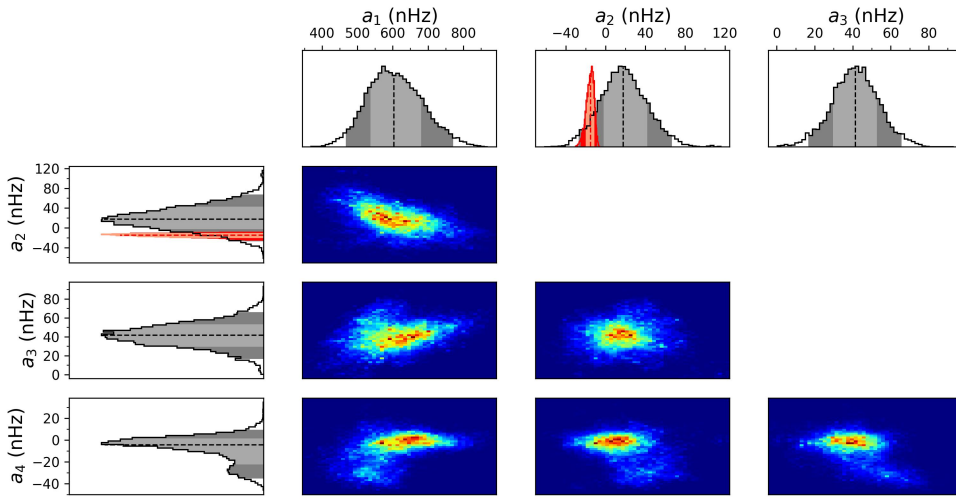


Fig. 12. Probability Density Functions and their correlations, obtained by MCMC of the power spectrum of 16 Cyg B and for coefficients a_1, a_2, a_3, a_4 for 16 Cyg A. The red curve shows the expected a_2^{CF} coefficient for a pure centrifugal distortion of the star. The light and dark gray PDF filling is for the 1σ and 2σ confidence interval, respectively.

540 two solutions. As our method of activity inference assumes Gaussian distributions, the bi-modality
 541 of a_4 requires to separate the two apparent solutions. Using Gaussian mixture modelling (Bishop
 542 1995; Bazot et al. 2019), the mean and standard deviation of both solutions are measured, enabling
 543 their separate analysis. The lowest estimate ($a_4 = -27.9 \pm 6.5\text{nHz}$) weights 30% and the highest
 544 estimate ($a_4 = -1.0 \pm 6.7\text{nHz}$) is more significant as it weights 70%. The inference of the activity
 545 from the two solutions is discussed in Section 6.4. Note that $a_3 = 45_{-14}^{+13}\text{nHz}$ is significantly higher
 546 than the reported values from Bazot et al. (2019) ($a_3 = 13.89 \pm 13.95\text{nHz}$) and may have an impact
 547 on the rotational profile.

548 6.3. Activity inference for 16 Cyg A

549 Figure 11 shows the results from the inference of the activity parameters and a statistical summary
 550 is in Table 3. Triangular and Gaussian descriptions of active latitudes give larger uncertainties than
 551 the simple gate model. However, they all suggest a near-equatorial activity, with a similar detection
 552 significance level of $\simeq 79\%$ (without bias correction) or $\simeq 96\%$ with fiducial correction. As for the
 553 Sun and because the shape of the active region is *a priori* unknown, the average distribution of the
 554 parameters are discussed. The activity intensity has a large uncertainty, but according to the median
 555 of ϵ , may be between the maximum and the minimum of solar activity.

556 The posterior probability distribution of δ does not allow us to precisely constrain the extension
 557 of the activity region. As already noted in the case of the Sun, this parameter requires stringent
 558 constraint on both the a_2 and a_4 coefficient in order to inform us about the size of the active region.

6.4. Activity inference for 16 Cyg B

559

Figure 13 and 14 shows the results for the activity for 16 Cyg B in the two possible scenarios of a_4 560
 discussed in Section 6.2 (see Table 3 for the statistical summary). In the case of $a_4 = -27.9 \pm 6.5 \text{ nHz}$ 561
 (Figure 13), the activity is highly significant (greater than 99.3% with or without bias correction, 562
 whatever is the activity zone model) and has stronger intensity than in the case of the Sun. The 563
 active region is then located at $\theta_0 \approx 58^\circ$ ($\theta_0 \approx 60^\circ$, after bias correction), ie. at comparable latitudes 564
 seen during a maximum of activity of the Sun. The bias correction has negligible effect on the 565
 inferred activity latitude. Due to a_4 significantly departing from 0, the extension of active region is 566
 better constrained than in 16 Cyg A or the Sun, but remains weakly informative. 567

The second more likely solution (probability of 70%) corresponds to $a_4 = -1.0 \pm 6.7 \text{ nHz}$ 568
 (Figure 14). It is associated to an activity at co-latitudes above $\approx 40^\circ$ and of lower activity. Its 569
 statistical significance is low, and the activity intensity may be of the same order or lower than 570
 16 Cyg A. In fact, it looks similar to the solar case when approaching its minimum of activity. 571
 Accounting for the fiducial bias, the solution is more concentrated to the equatorial region and 572
 differs significantly from the lower probability a_4 solution. Here, the uncertainty on a_2 and a_4 is 573
 again too large to provide a stringent constraint on the extension of the activity zone δ . 574

7. Discussion and Conclusion

575

The stellar activity is a complex phenomenon emerging from the interplay between the stellar 576
 plasma, rotation and magnetism. The activity distorts the shape of mode cavity, perturbing the 577
 pulsation frequencies. This perturbation is here observationally evaluated using a a-coefficient de- 578
 composition. This allows us to separate observables (the a-coefficients) from their physical inter- 579
 pretation (the activity modelling). The separation enables us to demonstrate that the measurements 580
 of the average low a-coefficient, a_2 and a_4 , under some observational conditions, are sufficient to 581
 reveal the presence of a statistically significant activity of similar intensity to the Sun and to deter- 582
 mine its latitude. The required observational conditions are analysed using a methodology similar 583
 to Kamiaka et al. (2018), that is, by constructing a grid of artificial power spectra, that allows us to 584
 determine the bias for a_1 , a_2 and a_4 . It is found that if the height-noise-ratio exceeds 10, the mode 585
 blending factor $f = a_1/\Gamma_{\nu_{max}}$ is greater than 0.4, the inclination is above 30° and that the observation 586
 is longer than 2 years, the inaccuracy remains mild and generally smaller than the 1σ uncertainty. 587
 The uncertainty and/or the inaccuracy may however become too large to reliably detect any activity 588
 beyond the above-specified conditions. In particular and in agreement with Kamiaka et al. (2018), 589
 the stellar inclination is a decisive variable to ensure the accuracy of the measurement. Below 30° , 590
 a_1 is often wrong by a factor 2. This is likely due to the fit mistakenly identifying $l = 2, m = \pm 1$ as 591
 $l = 2, m = \pm 2$ and vice-versa. Other a-coefficients are then severely inaccurate. Therefore, such a 592
 bias analysis suggests that rotation studies of stellar ensembles require a careful star selection. 593

A method that uses the average a_2 and a_4 coefficients is proposed to perform a subsequent 594
 analysis of the activity, considering a geometrical model of the activity effect on the pulsations 595

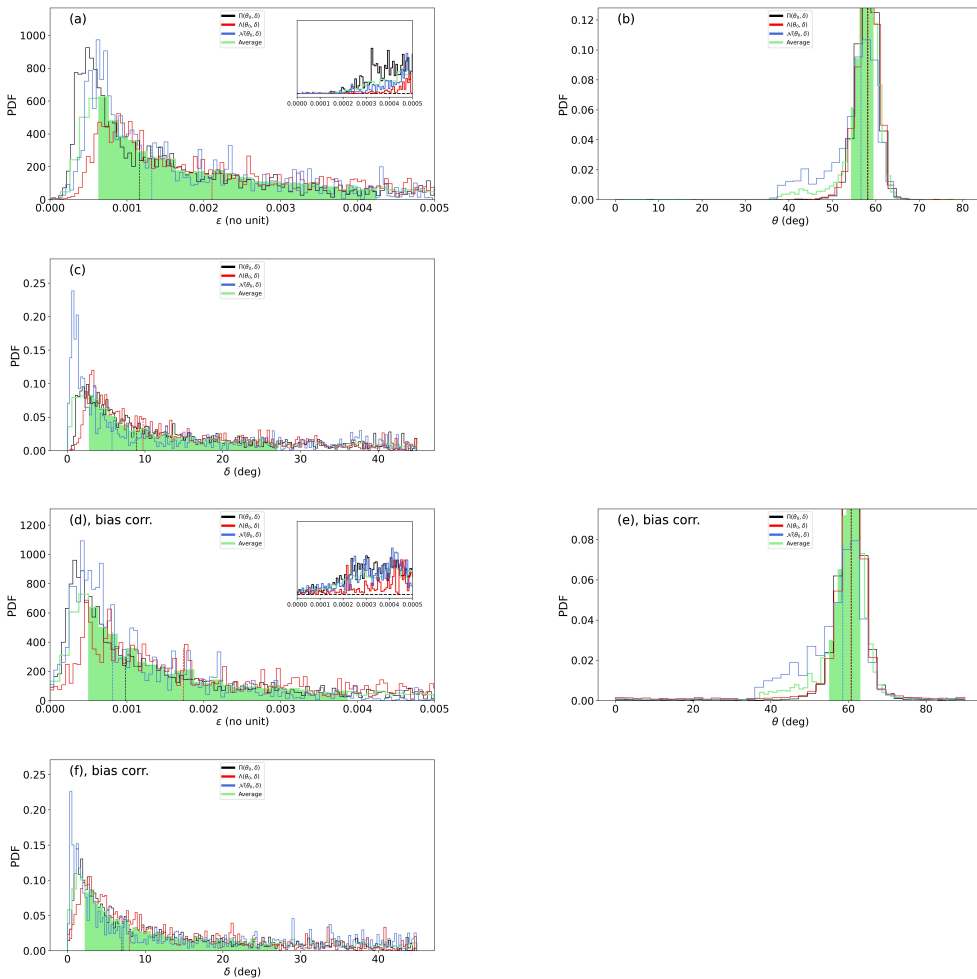


Fig. 13. Inferred pdf of ϵ , θ_0 and δ for raw results of 16 Cyg B with the lower solution $a_4 = -29.2 \pm 5.6\text{Hz}$, without bias correction (a, b, c) or with it (d, e, f). The green curve is for the average pdf with $F = \Pi$, Λ and N . The shaded area is its 1σ confidence interval. The inset of (a,d) is a zoom into the near-zero ϵ values with smaller binning.

596 frequencies and accounting for the stellar asphericity due to the centrifugal effects. This two-step
 597 approach is tested on the case of the Sun and shows that it is effectively able to detect the change
 598 of activity between the solar maximum of activity around 1999-2002 and the minimum of activity
 599 around 2006-2009. Although the use of averaged a-coefficients makes it difficult to evaluate the
 600 extension of the activity zone, the model successfully retrieves the mean latitude of activity during
 601 the maximum of the solar cycle.

602 The method is then applied to the brightest stars observed during the initial observational phase
 603 of the Kepler space instrument, 16 Cyg A and B. These stars were selected as a test-bed due to
 604 the fact that they are well studied and present the highest mode signal-to-noise ratio of all the
 605 currently known main-sequence stars. Davies et al. (2015) suggested that these stars have mild to
 606 no activity. However, Bazot et al. (2019), using a parametric model for describing the asphericity
 607 $(R_{\text{eq}} - R_{\text{pol}})/R_{\text{eq}}$ found an asphericity significant at 1σ . Our current analysis, performed using the
 608 same data set, confirms this asphericity and found a mild (relatively to the Sun) to moderate activity
 609 for both stars. It is found that 16 Cyg A has a near-equatorial band of activity during the period of

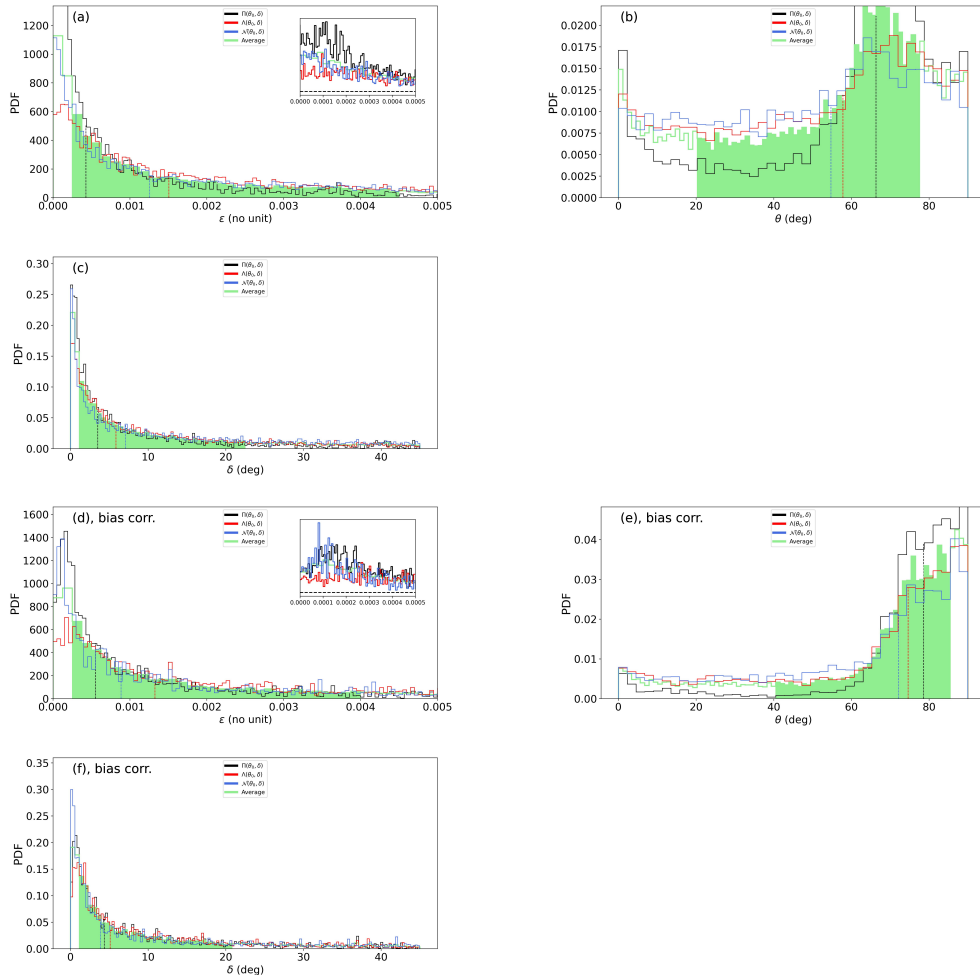


Fig. 14. Same as Figure 13 but for the higher solution $a_4 = -0.9 \pm 6.8\text{nHz}$.

observation (13 September 2010 to 8 March 2013), with a significance of the detection greater than 610
79.8%. 611

The case of 16 Cyg B is more ambiguous. A bi-modality on the average splitting $\langle \delta\nu_{nlm}/m \rangle \simeq a_1$ 612
and on the stellar inclination is already reported in Davies et al. (2015) and Bazot et al. (2019). 613
Our refined model suggests that this bi-modality is in fact related to the $l = 2$ modes. Indeed, as 614
we account for a_1 , a_2 , a_3 and a_4 , we note that the bi-modality previously seen on a_1 in earlier 615
studies is displaced to a_4 . The solutions of a_4 are separated using a Gaussian process algorithm, 616
which found that the weight (or importance) of the highest solution, close to 0 nHz is of 70%. 617
The lower solution, close to -28nHz has a weight of 30%. The associated probability distribution 618
for stellar inclination $i = 35 \pm 3$ is unique (instead of being bi-modal in past studies). The two 619
solutions of a_4 are analysed independently. The lower solution (with lower weight) is associated to 620
an overall activity that is stronger than the Sun, localised at latitudes of approximately 32° (with 621
an uncertainty of $\simeq 3^\circ$). The higher solution is linked to a lower activity and is weakly significant 622
(probability greater than 67.1%). Although the uncertainty is large, the study suggests an activity 623
closer to the equatorial region. In the Sun and as evident in its butterfly diagram, the quiet phase 624
is associated to a magnetic activity closer to the equator, while the transition to the active Sun is 625

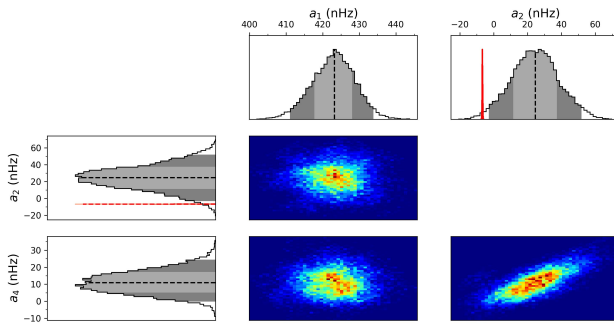


Fig. 15. Probability Density Functions and their correlations, obtained by MCMC for coefficients a_1 , a_2 , a_3 , a_4 for the Sun in-between two activity cycles (2006-2011). The red curve is the expected a_2^{CF} coefficient for a pure centrifugal distortion. The light and dark gray PDF filling is for the 1σ and 2σ confidence interval, respectively.

626 abrupt and characterised by the appearance of magnetic spots at latitudes of 30-40°. In that context
 627 and although it is not possible to rule out the possibility of a statistical fluke, an interpretation of the
 628 bi-modality is that the star was transitioning from a period of low activity to a more active period
 629 during the observation time of the Kepler instrument. To evaluate that hypothesis, we selected solar-
 630 data between Jan 2006 and Jan 2011, including the end of a cycle and the start of a new one. The
 631 measured a-coefficients for that analysis are shown in Figure 15. There is no visible bi-modality
 632 on either a_2 or a_4 . Because 16 Cyg B is evidently different than the Sun, this does not refute the
 633 hypothesis, but weakens it. A more firm verification would require a follow-up observation of the
 634 star, ie with PLATO (Rauer et al. 2014). Or extensive simulations in order to attempt to reproduce
 635 the bi-modality.

636 This work demonstrates that it is possible to determine the latitude and intensity of the activity
 637 for Sun-like stars, when this activity is similar to, or exceed the one of the Sun. The limited observed
 638 bias suggests that the analysis of the stellar activity could also be extended to a larger set of stars.
 639 The Kepler LEGACY stars (Lund et al. 2017) are ideal candidates as these generally satisfy the
 640 criteria of reliability that are discussed in this conclusion and detailed in Section 4.

641 Although the a-coefficient analysis has the benefit to allow to simplify the bias studies and to
 642 make the analysis faster, a further axis of improvement would consist in using a single analysis step,
 643 ie, fitting directly the power spectrum with the model of activity. Contrary to the two-step analysis,
 644 such an approach does not require assumptions on the properties of probability distribution of the
 645 a-coefficients as it is currently the case. It would also make use of the full set of a-coefficients
 646 (not only their average), which may lead to smaller uncertainties. However, the two approaches
 647 would certainly be needed in tandem, as the stability of the solution (and its accuracy) is harder to
 648 ascertain when performing a single step fitting approach.

649 O.B. and L.G. acknowledge partial support from NYUAD Institute Grant G1502 "Center for
 650 Space Science". L.G. is supported in part by the European Research Council (ERC) Synergy Grant
 651 WHOLE SUN 810218 and the Max Planck Society grant "Preparations for PLATO Science". We
 652 thank Saskia Hekker for comments and advice. All data presented in this paper were obtained from

the Mikulski Archive for Space Telescopes (MAST) at the Space Telescope Science Institute. The 653 specific observations analysed can be accessed via [10.17909/T9059R]<https://doi.org/10.17909/T9059R>

SOHO spacecraft, Kepler spacecraft

655

Analysis tool suite for this paper https://github.com/OthmanB/Benomar2022/tree/version_1

2

657

658 Appendix A: Polynomials, a-coefficients and splittings

659 A.1. The first six used polynomials

660 The $\mathcal{P}_j^{(l)}(m)$ coefficients, which are introduced by Schou et al. (1994), can be obtained by normal-
661 ising the $H_j^m(l)$ coefficients by Ritzwoller & Lavelle (1991) so that $\mathcal{P}_j^{(l)}(m = l) = l$.

$$\begin{aligned} \mathcal{P}_j^{(l)}(m) &= \frac{l(2l-j)!}{(2l)!} H_j^m(l) \\ &= (-1)^{-l+m} \frac{l \sqrt{(2l-j)!(2l+j+1)!}}{(2l)!} \begin{pmatrix} j & l & l \\ 0 & m & -m \end{pmatrix} \end{aligned} \quad (\text{A.1})$$

662 in which the last factor means the Wigner $3j$ symbol.

663 They can also be obtained by recurrence using equation (2) and (3), together with the normali-
664 sation condition, $\mathcal{P}_j^l(m) = l$ and starting with $\mathcal{P}_0^l(m) = l$.

665 The first six polynomials are as follows:

$$\mathcal{P}_1^{(l)}(m) = m \quad (\text{A.2})$$

666

$$\mathcal{P}_2^{(l)}(m) = \frac{3m^2 - l(l+1)}{2l-1} \quad (\text{A.3})$$

667

$$\mathcal{P}_3^{(l)}(m) = \frac{5m^3 - (3l(l+1)-1)m}{(l-1)(2l-1)} \quad (\text{A.4})$$

668

$$\mathcal{P}_4^{(l)}(m) = \frac{(35m^4 - 5(6l(l+1)-5)m^2) + 3l(l+1)(l(l+1)-2)}{2(l-1)(2l-1)(2l-3)} \quad (\text{A.5})$$

669

$$\mathcal{P}_5^{(l)}(m) = \frac{252m^5 - 140(2l-3)m^3 + (20l(3l-10)+48)m}{8(4l^4 - 20l^3 + 35l^2 - 25l + 6)} \quad (\text{A.6})$$

$$\begin{aligned} \mathcal{P}_6^{(l)}(m) &= \frac{924m^6 - 420m^4(3l-7) + 84m^2(5l^2 - 25l + 14)}{N} \\ &\quad - \frac{20l(L^2 - 8L + 12)}{N} \end{aligned} \quad (\text{A.7})$$

670 where $L = l(l+1)$ and $N = 64l^5 - 480l^4 + 1360l^3 - 1800l^2 + 1096l - 240$.

A.2. Relationship between a-coefficients and splittings

671

The relationships between a-coefficients and symmetric/anti-symmetric splittings can be derived 672
using equations (4) and (5). These are used to convert model frequencies ν_{nlm} into a-coefficients. 673

A.2.1. Explicit form for low a-coefficients and l=1

674

$$a_1(n, l = 1) = S_{n11} = \frac{\nu_{n,1,1} - \nu_{n,1,-1}}{2} \quad (\text{A.8})$$

675

$$a_2(n, l = 1) = T_{n11}/3 = \frac{(\nu_{n,l,-1} + \nu_{n,l,1})/2 - \nu_{n,l,0}}{3} \quad (\text{A.9})$$

A.2.2. Explicit form for low a-coefficients and l=2

676

$$a_1(n, l = 2) = \frac{S_{n21} + 4S_{n22}}{5} \quad (\text{A.10})$$

677

$$a_2(n, l = 2) = \frac{2T_{n22} - T_{n21}}{7} \quad (\text{A.11})$$

678

$$a_3(n, l = 2) = \frac{S_{n22} - S_{n21}}{5} \quad (\text{A.12})$$

679

$$a_4(n, l = 2) = \frac{T_{n22} - 4T_{n21}}{70} \quad (\text{A.13})$$

A.2.3. Explicit form for low a-coefficients and l=3

680

$$a_1(n, l = 3) = \frac{S_{n31} + 4S_{n32} + 9S_{n33}}{14} \quad (\text{A.14})$$

681

$$a_2(n, l = 3) = \frac{-15T_{n31} + 25T_{n33}}{126} \quad (\text{A.15})$$

682

$$a_3(n, l = 3) = \frac{-S_{n31} - 2S_{n32} + 3S_{n33}}{9} \quad (\text{A.16})$$

683

$$a_4(n, l = 3) = \frac{T_{n31} - 7T_{n32} + 3T_{n33}}{77} \quad (\text{A.17})$$

$$a_5(n, l = 3) = \frac{5S_{n31} - 8S_{n32} + 3S_{n33}}{126} \quad (\text{A.18})$$

$$a_6(n, l = 3) = \frac{15T_{n31} - 6T_{n32} + T_{n33}}{1386} \quad (\text{A.19})$$

686 **Appendix B: Spectrum analysis**687 *B.1. Acoustic-spectrum modelling*

688 The analysis of the asteroseismic data is very often performed by fitting the power spectrum (eg.
 689 Appourchaux et al. 1998, 2008). This requires to devise a likelihood function and a model for the
 690 observed spectrum. As our fitting involves a Bayesian approach, the priors are also required.

691 *B.1.1. Likelihood*

692 The likelihood function is determined by the noise statistics of the power spectrum, which is a χ^2 -
 693 squared with two degree of freedom. It is also based on the assumption that the frequency bins are
 694 independent and uncorrelated. This implies that the observation duration is assumed to be much
 695 greater than the typical lifetime of the pulsation modes and that the duty cycle is sufficient to allow
 696 us to neglect any leakage induced by the window function. The observation timeframe for the
 697 LEGACY sample is of the order of years, which is significantly longer than the mode lifetime.
 698 Furthermore, the duty cycle is above 95%, which was shown to be sufficient to neglect leakage
 699 (Stahn 2010). Under these conditions, the likelihood function is (Anderson et al. 1990),

$$L_1(S(\nu_i)|X, M) = \sum_{i=0}^{N-1} \frac{1}{S(\nu_i)} \exp\left(-\frac{S(\nu_i)}{M(\nu_i, X)}\right) \quad (\text{B.1})$$

700 where $S(\nu_i)$ is the power at the central frequency ν_i of the i^{th} bin. Here, N is the total number of
 701 bins and $M(\nu_i, X)$ is the model of the power spectrum with the set of variable X for the model M .

702 From Bayes theorem, the posterior probability density function is defined as,

$$\pi_1(X|S(\nu), M) = \frac{\pi_1(X|M) L_1(S(\nu)|X, M)}{\pi_1(S(\nu)|M)} \quad (\text{B.2})$$

703 where $\pi_1(X|M)$ is the prior knowledge on the parameters X . $\pi_1(S(\nu)|M)$ is a normalisation constant,
 704 essential only for comparing the significance of models (eg. Gregory 2005; Benomar et al. 2009).
 705 Variables are assumed to be independent from each others. This implies that the joint prior is the
 706 product of individual priors. The posterior is evaluated using the Tempered Adaptive MCMC code¹⁰
 707 described in Atchadé (2006) and implemented by Benomar (2008).

¹⁰<https://github.com/OthmanB/Benomar2022/Programs/TAMCMC-1.81>

| | |
|--------------------------------|-----|
| B.1.2. Acoustic spectrum model | 708 |
|--------------------------------|-----|

The model used for the power spectrum fitting, involves a sum of asymmetrical Lorentzian, superimposed to a monotonically decreasing function of frequency (pink noise). The asymmetric Lorentzian is commonly used in helioseismology (Duvall et al. 1993; Nigam & Kosovichev 1998; Georgobiani et al. 2000; Toutain et al. 1998) and in asteroseismology for Sun-like stars (Benomar et al. 2018b),

$$M(\nu) = \sum_{n=n_0}^{n_{\max}} H_{nlm} \frac{(1 + B_{nlm} z)^2 + B_{nlm}^2}{1 + z^2} + N(\nu), \quad (\text{B.3})$$

with $z = 2(\nu - \nu_{nlm})/\Gamma_{nlm}$. Each asymmetrical Lorentzian is defined by a height H_{nlm} , width Γ_{nlm} , a central frequency ν_{nlm} and an asymmetry B_{nlm} . As explained by Gizon (2006); Benomar et al. (2018b), the asymmetry coefficient depends on the mode width and frequency. The normalised asymmetry coefficient $\chi_{nlm} = 2 \frac{B_{nlm} \nu_{nlm}}{\Gamma_{nlm}}$ is fitted instead as it is nearly constant over the range of fitted modes.

Several prescriptions exist for describing the noise background $N(\nu)$. Here, it is assumed to be a sum of two generalised Lorentzian, sometimes referred as Harvey-like profiles (Harvey 1985), and of a white noise,

$$N(\nu) = \frac{A_1}{1 + (\tau_1 \nu)^{p_1}} + \frac{A_2}{1 + (\tau_2 \nu)^{p_2}} + N_0. \quad (\text{B.4})$$

Here N_0 is the white noise and A_k is the maximum heights of the k^{th} generalised Lorentzian. The τ_k parameter is timescale that is the inverse of the full width at half maximum of the Lorentzians, and p_k is a power exponent.

The fit is performed globally over all the statistically significant peaks visible in the power spectrum of a star. This can lead to a very large number of fitted parameters (up to a few thousands), which is practically unsuitable. A model simplification is therefore preferred, similar to eg. Appourchaux et al. (2008); Benomar et al. (2009); Campante et al. (2011); Handberg & Campante (2011) with main simplifications recalled hereafter,

- The m dependence on heights is controlled by its relationship with the stellar inclination (Gizon & Solanki 2003). This saves several hundreds of parameters.
- The relative height of the different degree l is constant across the fitted range and for a given l , hence $V_l^2 = H_{n,l}/H_{n,l=0} = \text{const}$. Only the $l = 0$ heights $H_{n,l=0}$ are variables. The mode visibility V_l^2 replaces the $H_{n,l>0}$ as a variable.
- Given a degree l , $\Gamma_{n,l,m} = \Gamma_{n,l}$ is imposed. This is justified by the fact that the width depends weakly on the frequency: all split components are assumed to have the same width.
- Because $\Gamma_{n,l}$ is nearly independent of the degree, it is possible to fit $\Gamma(\nu) = \Gamma_{n,l=0}$ and interpolate it to the frequencies of the modes with degree $l > 0$.

These assumptions reduce the number of variables to a few tens in the case of CoRoT, Kepler or TESS observations. The frequencies of the modes follow equation (14) in Section 2.3.

741 **B.2. Priors**

742 Priors are fundamental of a Bayesian method. This section explicits $\pi_1(X|M, I)$, the prior used
 743 during the power spectrum fitting. Parameters of the vector X are assumed independent to each
 744 others, such that the product rule is used to define $\pi_1(X|M, I)$.

Table B.1. Mode priors used for the fit of the power spectrum. Prior parameters on frequencies are visually determined, see Section B.2.

| Main mode parameters | | | | | | |
|---------------------------|------------------------|---------------------------------------|------------------------|--------------------------|----------------------------|---------------------|
| Height ($ppm^2/\mu Hz$) | Width (μHz) | Frequency (μHz) | Asymmetry ($ \chi $) | $V_{l=1}^2$ | $V_{l=2}^2$ | inclination |
| $\mathcal{J}(1,1000)$ | $\mathcal{J}(0.1, 45)$ | $\mathcal{U}(\nu_{\min}, \nu_{\max})$ | $\mathcal{J}(5, 100)$ | $\mathcal{G}(1.5, 0.15)$ | $\mathcal{G}(0.53, 0.053)$ | $\mathcal{U}(0,90)$ |

745 Heights, widths, frequencies, asymmetry and inclination use non-informative priors. These are
 746 either Jeffreys priors for scale parameters, noted $\mathcal{J}(x_{\min}, x_{\max})$ or uniform prior, noted $\mathcal{U}(x_{\min}, x_{\max})$.
 747 Priors on frequencies are uniform and require a visual inspection of the power spectrum in order to
 748 assign the lower and upper bound of the prior for each mode that follow the expected pattern for
 749 main sequence Sun-like stars (equally spaced p modes) and that show an excess of power relative
 750 to the background that exceeds 80%. The excess of power is determined using a smooth spectrum
 751 for which the noise statistics is derived by Appourchaux (2003). Mode visibilities are defined by
 752 Gaussian priors (noted $\mathcal{G}(x_0, \sigma)$), with mean x_0 set as the solar value (see Ballot et al. 2011) and
 753 the standard deviation σ is 10% of the mean. Table B.1 lists the type and the prior characteristic
 754 values that are used for the parameters of the modes.

755 The prior on a_1 is uniform between 0 and 1500 nHz. For 16 Cyg A and B, an uniform fixed prior
 756 is set on $|a_3|$ over the range [0, 100] nHz. However at each iteration of the optimisation process, $|a_3|$
 757 is not allowed to exceed 20% of a_1 . Preventing extremely large relative value of a_3/a_1 , improves
 758 the fit stability and ensure a faster convergence of the algorithm. For the Sun analysis and because
 759 it is not possible to measure a_3 for $i \approx 90^\circ$ (due to the lack of amplitude of $l = 2, m = \pm 1$ at that
 760 inclination), a_3 is fixed to 0.

761 The priors on a_2 and a_4 are also uniform. The range is defined by using the maximum range
 762 of Figure 3 (showing $a_2^{(AR)}$ and $a_4^{(AR)}$), increasing it by 50% and adding the expected centrifugal
 763 term $a_2^{(CF)}$, assuming $a_1 = 400$ nHz for the Sun and $a_1 = 600$ nHz for 16 Cyg A/B. The $\Delta\nu$ reported
 764 in Table 2 is also used. For the same reason as to a_3 , a_2/a_1 cannot exceed 50% and a_4/a_1 cannot
 765 exceed 20% at each iteration step of the optimisation process.

766 The noise priors are obtained from a global MAP approach similar to Benomar et al. (2012).
 767 This provides the best fit values and 1σ uncertainties that are used as priors. The noise background
 768 of the individual model analysis is described by equation (B.4). During the global MAP fit, the
 769 model is made of that same background model, plus a Gaussian envelope to account for the power
 770 excess due to the modes (eg Mathur et al. 2010; Huber et al. 2011).

Appendix C: Inference of the active latitudes

771

The determination of the activity is performed as a second step using as observables the marginalised posterior distribution of the average a-coefficients. This section describes the method and assumptions to determine the posterior distribution and to compute the significance of the detection. 772
773
774

C.1. Posterior distribution and likelihood

775

Similarly as to the power spectrum fitting described in Section B, the determination of the most likely latitudes for the activity and its significance necessitate the computation of a posterior distribution, 776
777
778

$$\pi_2(\mathbf{X}|\mathbf{O}, M) = \frac{\pi_2(\mathbf{X}|M) L_2(\mathbf{O}|\mathbf{X}, M)}{\pi_2(\mathbf{O}|M)}, \quad (\text{C.1})$$

with $\pi_2(\mathbf{X}|\mathbf{O}, M)$, $\pi_2(\mathbf{X}|M)$, $L_2(\mathbf{O}|\mathbf{X}, M)$ are the posterior distribution, the prior, the likelihood, respectively. The denominator $\pi_2(\mathbf{O}|M)$ is the normalisation constant used for model comparison (marginal likelihood). The posterior distributions of the a-coefficients $a_{2,o}$ and $a_{4,o}$ obtained by power spectrum fitting are the observables contained in \mathbf{O} . The class of the model is identified by the variable M . 779
780
781
782
783

For simplicity, the observables are assumed to be distributed according to un-correlated Gaussian functions, such that $\mathbf{O} = \{a_{2,o}, a_{4,o}, \sigma_{2,o}, \sigma_{4,o}\}$, where $a_{2,o}$ and $a_{4,o}$ are the mean for the distributions of a_2 and a_4 while $\sigma_{2,o}$, $\sigma_{4,o}$ are the standard deviations. This leads to a log-Likelihood in the form of a χ^2 -squared, 784
785
786
787

$$\ln L_2(\mathbf{X}|\mathbf{O}, M) = -\frac{(a_{2,o} - a_{2,m}(\mathbf{X}))^2}{2\sigma_{2,o}^2} - \frac{(a_{4,o} - a_{4,m}(\mathbf{X}))^2}{2\sigma_{4,o}^2}. \quad (\text{C.2})$$

In Dziembowski et al. (2000), a-coefficients are weighted using the inverse of the mode inertia (see their equation 4). This is due to the fact that the inertia account for most of the frequency-variations of the coefficients. It is essentially relevant if the uncertainties are small enough to observe a trend when modes are fitted individually. However, in the case of the Sun and with either GOLF or BiSON data, it is difficult to perceive a frequency-trend (Chaplin et al. 2003). Our own trials on VIRGO/SPM using a linear fit to describe the frequency dependence of a-coefficient did not detect a slope that is significant at more than 1σ . A similar analysis on 16 Cyg A and B and on simulations showed evidence of large uncertainties when attempting to determine frequency-variations for stars with HNR typical of Kepler observations. In fact, only the average the a-coefficient over l and n is shown to be robustly determined (see also our discussion Section 3.3) so that inertia effects are here neglected. 788
789
790
791
792
793
794
795
796
797
798

799 The activity model M_{AR} depends on the variables $\mathbf{X} = \{\epsilon, \theta_0, \delta\}$ and $a_{2,m}(\mathbf{X})$, $a_{4,m}(\mathbf{X})$ denote the
800 modelled a-coefficients. The log-likelihood is then,

$$\begin{aligned} \ln L_2(a_{2,o}, a_{4,o}, \sigma_{2,o}, \sigma_{4,o} | a_{2,m}, a_{4,m}, M_{AR}) = \\ - \frac{(a_{2,o} - a_{2,m}(\epsilon, \theta_0, \delta))^2}{2\sigma_{2,o}^2} \\ - \frac{(a_{4,o} - a_{4,m}(\epsilon, \theta_0, \delta))^2}{2\sigma_{4,o}^2}. \end{aligned} \quad (\text{C.3})$$

801 In our case, the observables are the average of the fitted modes coefficients, $a_{2,o} = a_2^{(CF)} + a_2^{(AR)}$
802 and $a_{4,o} = a_4^{(AR)} = 0$. However, to conveniently propagate all errors on the parameters of $a_2^{(CF)}$
803 ($a_1, \Delta\nu, \Delta\nu_\odot, \rho_\odot, \nu_{nl}$), it is preferable to use $a_{2,o} = a_2^{(AR)}$, obtained by subtracting the $a_2^{(CF)}$ from
804 the a_2 measured by power spectrum fitting. The distribution of $\Delta\nu$ is computed by linear fitting
805 of the group-wise ensemble of samples ($n, l = 0$) for each measured frequencies ν_{n0} . The term
806 $a_2^{(CF)}$ is finally obtained by weighted average of all independent $a_2^{(CF)}(n, l)$ computed at the star's
807 posterior frequencies ν_{nl} . The subtraction of $a_2^{(CF)}$ is then again performed using the samples of
808 its posterior, enabling to construct of the posterior probability distribution function of $a_2^{(AR)}$, from
809 which we deduce its mean $a_{2,o}$ and its standard deviation $\sigma_{2,o}$. To evaluate the relevance of the
810 activity, two models are considered. First, a model ($M = M_{CF}$) without activity, that accounts only
811 for the centrifugal effects and second, a model ($M = M_{AR}$) with activity. Their details and the
812 choice of the priors is described in the following sections for each of them.

813 C.2. Model without activity M_{CF}

814 The model M_{CF} has no unknown variable that require minimisation, see equation (13). For the sake
815 of the model comparison with the model M_{AR} , it is however important to determine the marginal
816 likelihood of M_{CF} . From that perspective, it is necessary to calculate the denominator of equation
817 (C.1), $P(\mathbf{O}|M_{CF})$ which is defined as an integral,

$$P(\mathbf{O}|M_{CF}) = \int \pi(\mathbf{X}|M_{CF}) L_2(\mathbf{O}|a_{2,m}, a_{4,m}, M_{CF}) d\mathbf{X}. \quad (\text{C.4})$$

818 An absence of activity correspond to the limit case where the a-coefficients of the activity are
819 exactly 0. This corresponds to setting Dirac priors on $a_{2,m} = \delta_0$ and $a_{4,m} = \delta_0$ and implies that
820 the marginal likelihood is the local value of the likelihood at $\mathbf{X} = \{0, 0\}$. The model comparison is
821 commonly performed in log-space such that,

$$\ln P(a_{2,o}, a_{4,o}, \sigma_{2,o}, \sigma_{4,o} | M_{CF}) = -\frac{a_{2,o}^2}{2\sigma_{2,o}^2} - \frac{a_{4,o}^2}{2\sigma_{4,o}^2}. \quad (\text{C.5})$$

| | |
|-----------------------------------|-----|
| C.3. Model with activity M_{AR} | 822 |
|-----------------------------------|-----|

Regarding the model with activity of equation (C.3), priors must then be set on the variables subject to optimisation. The ϵ and δ parameters are indispensable intensive parameters and the adequate non-informative prior is then the (truncated) Jeffreys prior (Jeffreys 1961), uniform in the log-space, 823
824
825
826

$$J(x) = \frac{\ln(1 + x_{max}/x_{min})}{x + x_{min}}, \quad (\text{C.6})$$

where x_{min} , x_{max} are upper and lower bounds such that if $x > x_{max}$ or $x < x_{min}$ then $J(x) = 0$. 827
This guarantees that the probability density is proper (the integral over x is finite). In case of weak 828
information content in the observables, this prior is more weighted toward a null-value. We set 829
 $\epsilon_{min} = 5.10^{-4}$ and $\epsilon_{max} = 10^{-2}$. This embraces the solar value $\epsilon \simeq 5.10^{-4}$ (Gizon 2002). Because 830
at the maximum of solar activity, $\delta \simeq 10^\circ$, we set $\delta_{min} = 10^\circ$. Note also that consistently with the 831
discussion on Figure 2 of Section 3, $\delta_{max} = 45^\circ$ is required. 832

Finally, the location parameter θ_0 has an uniform prior in the range $[0, 90]^\circ$. 833

The marginal likelihood of the model M_{AR} requires us to evaluate the triple integral, 834

$$P(\mathbf{O}|M) = \int \pi(\epsilon) \pi(\theta) \pi(\delta) L_2(\mathbf{O}|a_{2,m}, a_{4,m}, M) d\epsilon d\theta d\delta. \quad (\text{C.7})$$

The MCMC process used here involves the use of parallel Metropolis-Hastings tempered chains. 835
The chains are mixing each other in order to enhance the sampling. As explained in Benomar 836
et al. 2009, see their Section A.3, these parallel chains can be used to approximate the equation 837
(C.7). This technique is here used with 10 parallel chains following a geometrical temperature law 838
 $T_k = 1.7^{k-1}$, with k , the chain index such that $k = 1$ is the target distribution, given by equation 839
(C.1). 840

Appendix D: Bias map for $\widehat{HNR} = 10$ and $\widehat{HNR} = 20$

This section shows the bias on the a_1 , a_2 and a_4 coefficients in the case of $\widehat{HNR} = 10$ or $\widehat{HNR} = 20$. The figure D.1 and D.3 are for the case of an equatorial band of activity and figure D.2 and 842
843
844
845
846
847
848
849
850

D.4, for a polar cap. It is noticeable that the inaccuracy of the fit remains smaller than standard deviation in the majority of the parameter space and for $i > 30^\circ$, $a_1/\Gamma_{v_{max}} > 0.4$. Interestingly, the relative-to-error bias on a_1 is more pronounced in the case of an equatorial band of activity and for $\{a_1/\Gamma_{v_{max}} \leq 0.4, i = [30, 60]\}$ (Figure D.1d and D.3d) and can exceed 3 times the uncertainty. The accuracy of the inference of activity based on the a-coefficients is expected to weakly depend on the \widehat{HNR} (although potentially with large uncertainty) for most stars, except within this regime (in addition to the gray area), where the centrifugal effect will be overestimated.

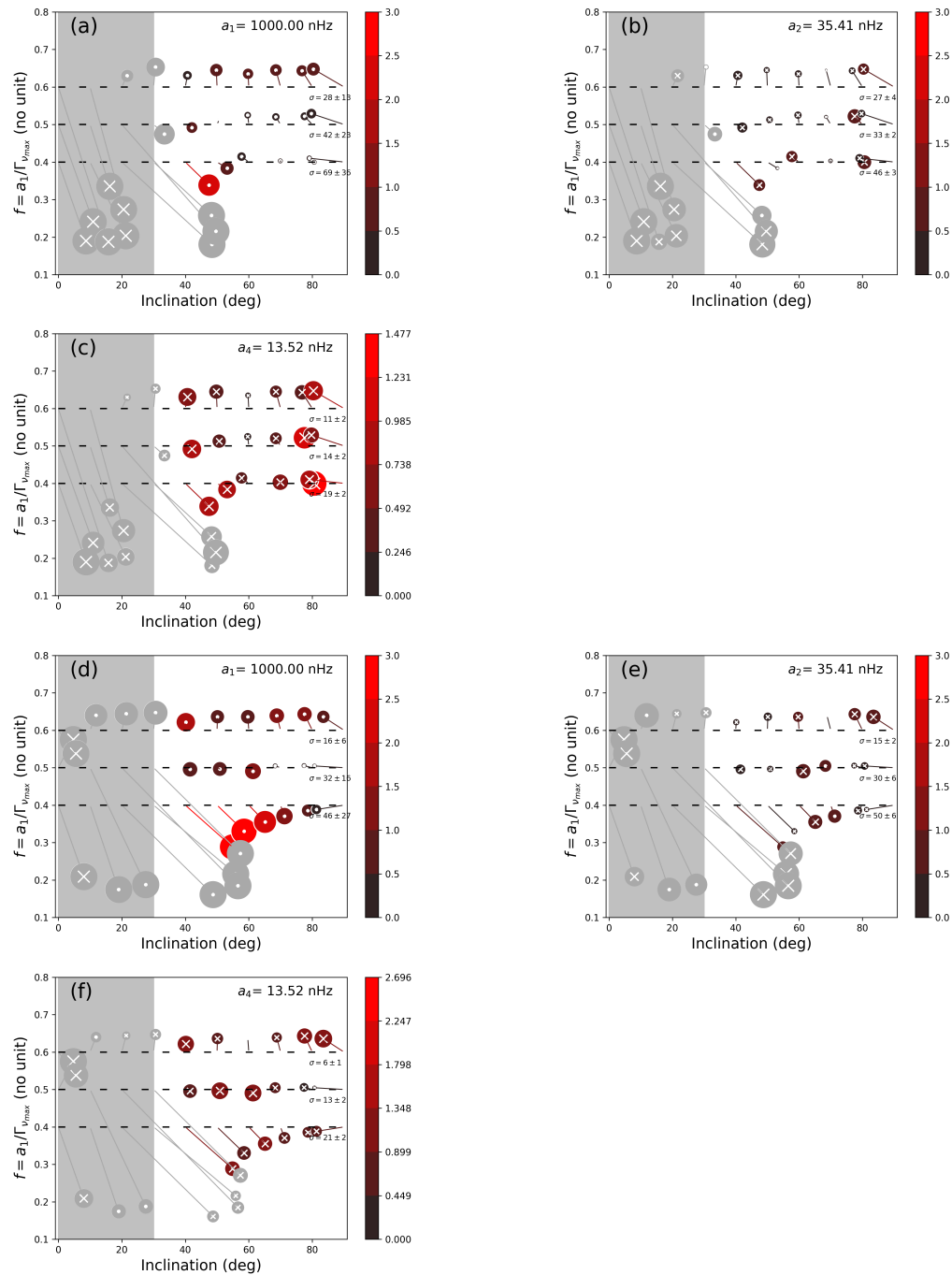


Fig. D.1. Bias analysis for $\widehat{HNR} = 10$ for an equatorial activity band ($\theta_0 = 85, \delta = 10$) of similar intensity to the Sun ($\epsilon_{nl} = 5.10^{-4}$), for $T_{obs} = 2$ years (top) and $T_{obs} = 4$ years (bottom).

851 Appendix E: Figures of the best fits

852 This section presents visuals on the best MCMC fits for the power spectrum of the active Sun
 853 (Figure E.1), quiet Sun (Figure E.2), 16 Cyg A (Figure E.3) and for the two a_4 solutions of 16 Cyg
 854 B (Figures E.4 and E.5). For 16 Cyg B, the solutions are here separated by selecting the median
 855 for the samples only below or above $a_4 = 21\text{nHz}$. In the case of the Sun, the impact of the activity
 856 on the profile of $l = 2$ is very clear, as the shifts of the m-components introduces an asymmetry in

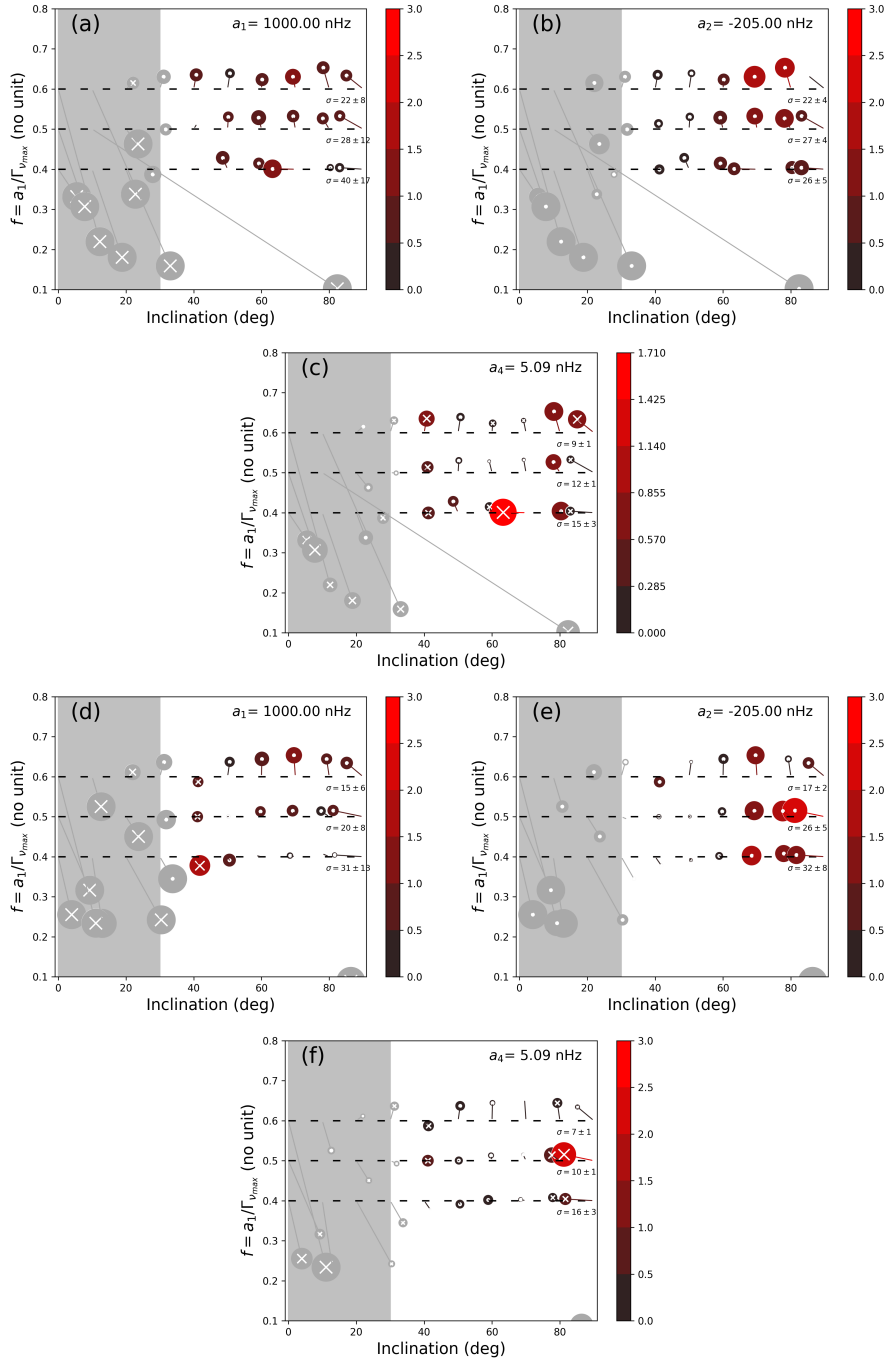


Fig. D.2. Bias analysis for $\widehat{HNR} = 10$ for a large polar activity cap ($\theta_0 = 22.5^\circ, \delta = 45^\circ$) of similar intensity to the Sun ($\epsilon_{nl} = 5.10^{-4}$), for $T_{obs} = 2$ years (top) and $T_{obs} = 4$ years (bottom).

power for the overall $l = 2$ mode profile during the active phase. During the quiet phase such an asymmetry is not visible. 857

Similarly and although it is less pronounced than in the Sun, in the case of 16 Cyg A and B, a weak asymmetry is visible on $l = 2$ modes. For 16 Cyg B, the two solutions of a_4 provide sensibly similar mode profiles as the difference is weakly apparent to the eye only for $l = 2$. The residuals do not show striking differences. This visually supports the fact that goodness of the fit is similar and explain that the two solutions co-exists in statistical terms. 859
860
861
862
863

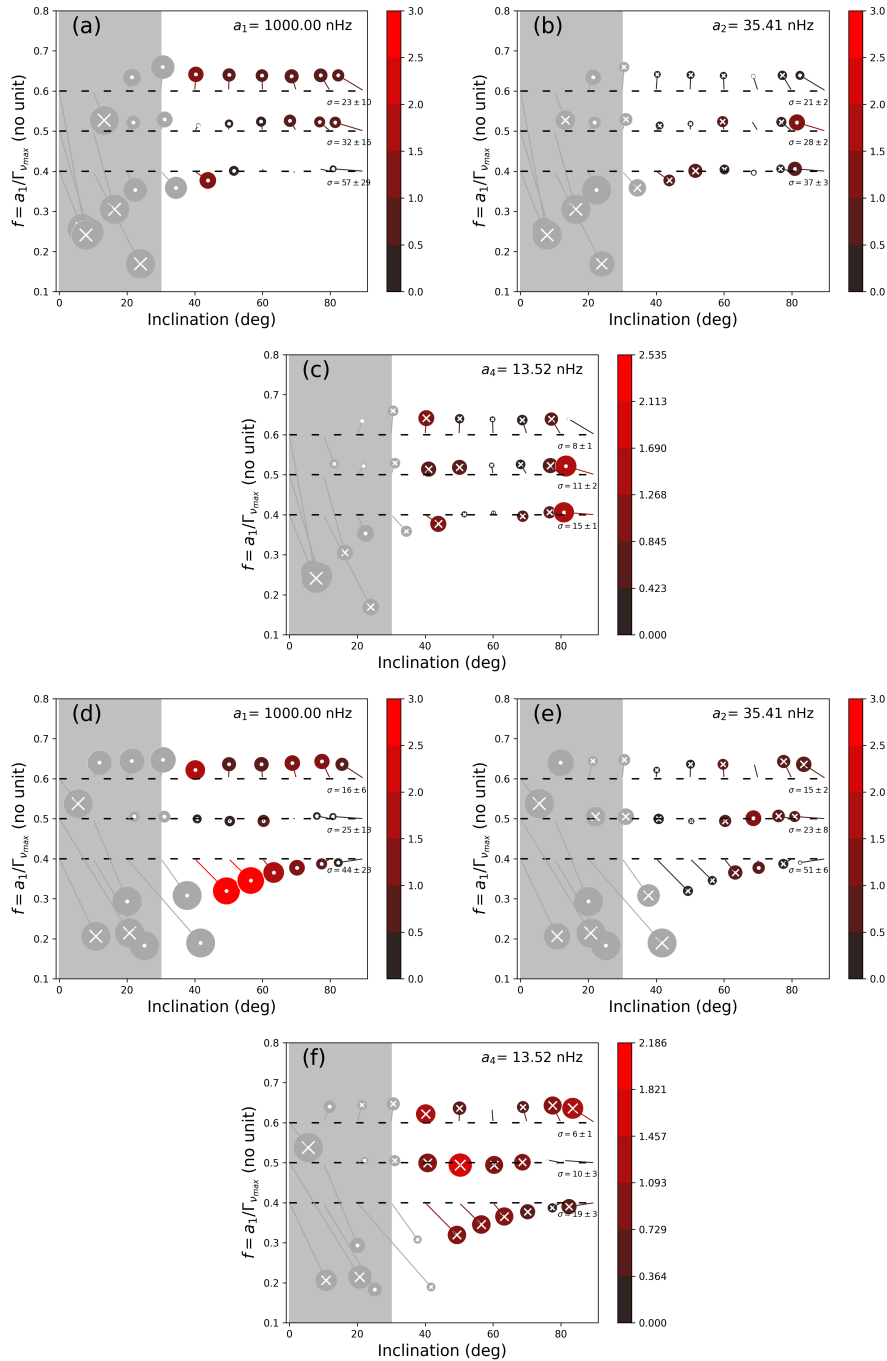


Fig. D.3. Bias analysis for $\widehat{HNR} = 20$ for an equatorial activity band ($\theta_0 = 85, \delta = 10$) of similar intensity to the Sun ($\epsilon_{nl} = 5.10^{-4}$), for $T_{obs} = 2$ years (top) and $T_{obs} = 4$ years (bottom).

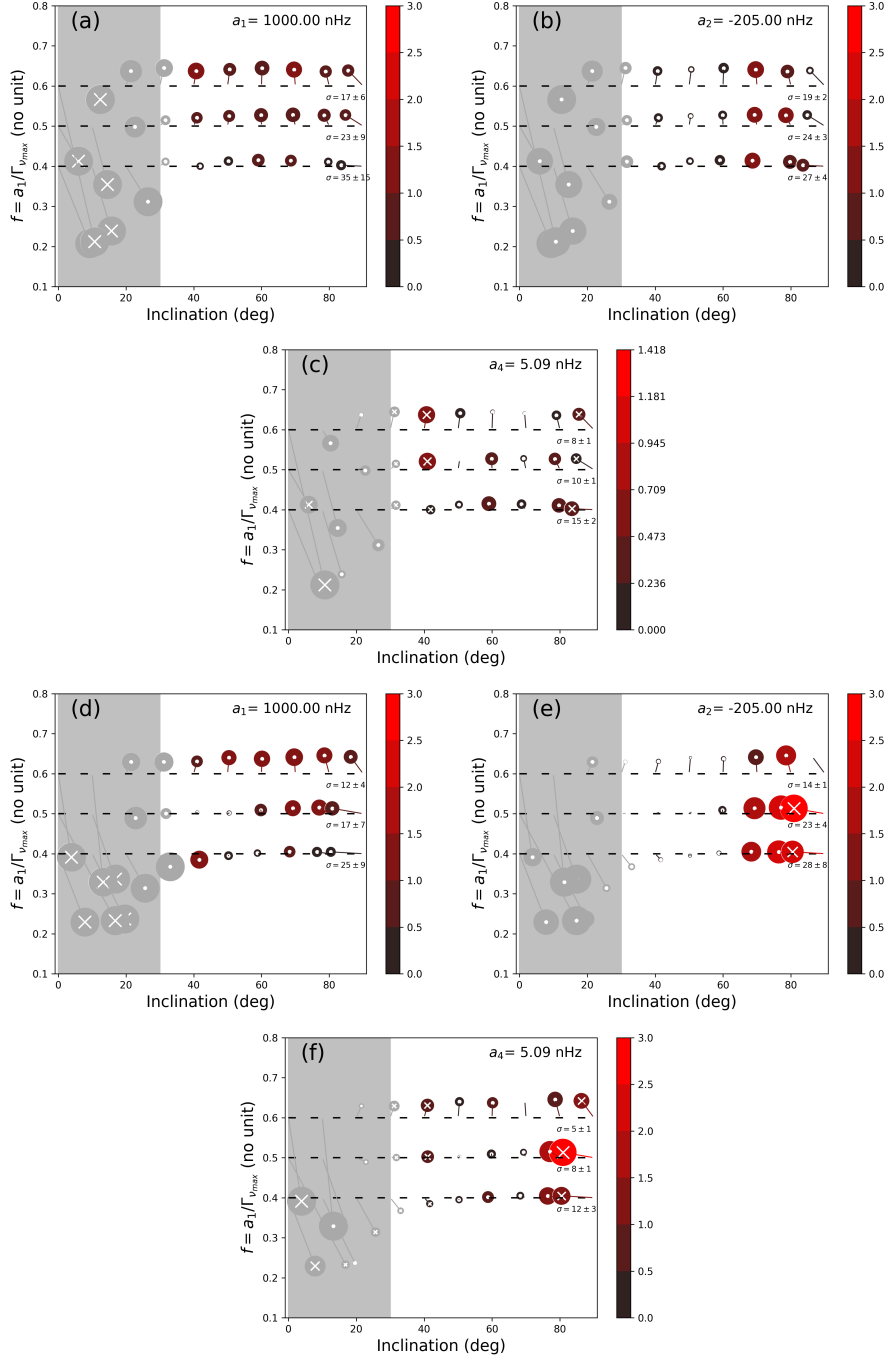


Fig. D.4. Bias analysis for $\widehat{HNR} = 20$ for a large polar activity cap ($\theta_0 = 22.5, \delta = 45$) of similar intensity to the Sun ($\epsilon_{nl} = 5.10^{-4}$), for $T_{obs} = 2$ years (top) and $T_{obs} = 4$ years (bottom).

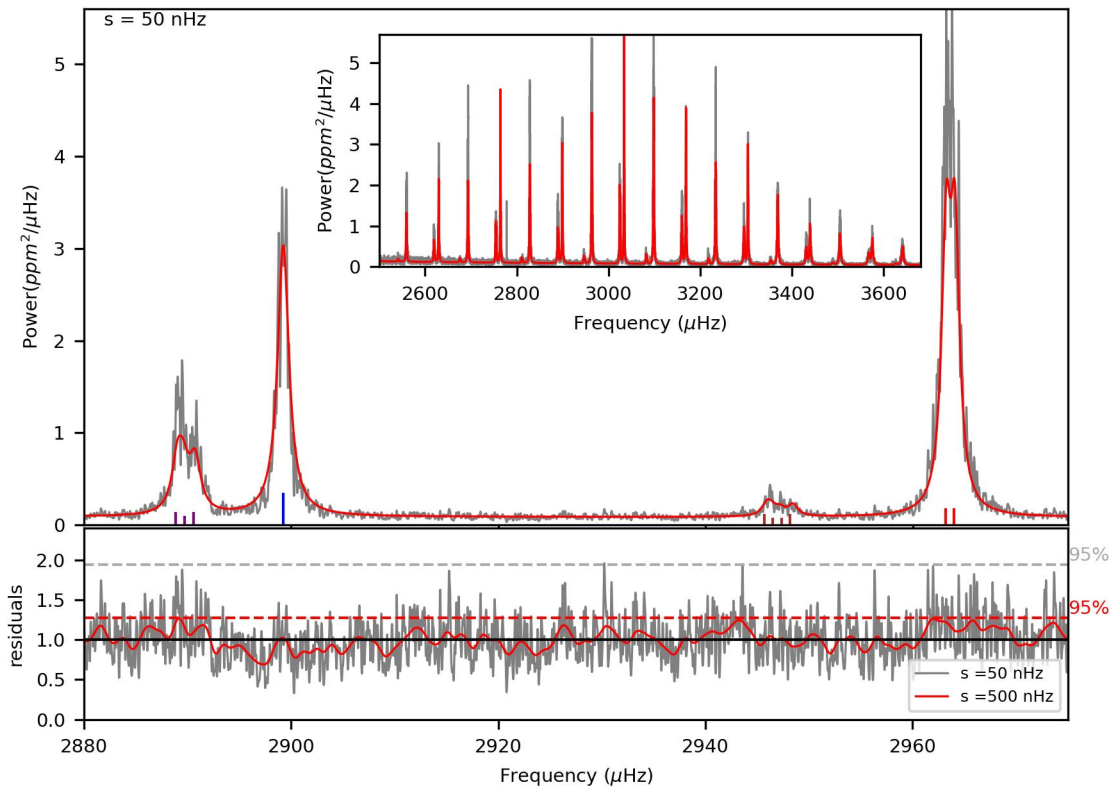


Fig. E.1. Solar power spectrum for observation between 1999 and 2002 after Gaussian smoothing over a kernel width $s=50\text{ nHz}$. Superimposed is the best MCMC fit. Top. Highlight of a $l = 2, 0, 3, 1$ mode group (left to right) and their fit (red). The power asymmetry due to non-symmetric m components is visible in the data. Inset. Overall view of the modes. Bottom. Residual of the fit with two level s of Gaussian smoothing.

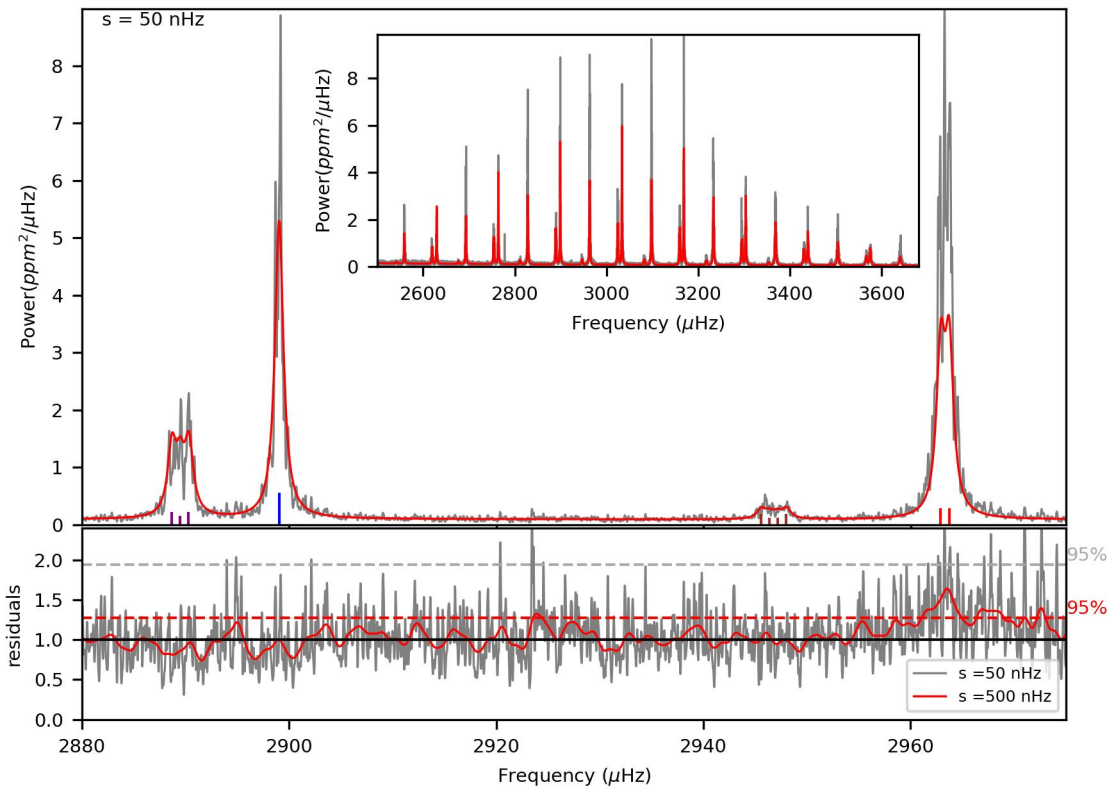


Fig. E.2. Same as Figure E.1 but between 2006 and 2009. Top. Highlight of a $l = 2, 0, 3, 1$ mode group (left to right) and their fit (red). The power asymmetry seen for 1999–2002 is not apparent in the data. Inset. Overall view of the power spectrum. Bottom. Residual of the fit with two level s of Gaussian smoothing. The residual on $l = 1$ is a bit high here due to the fix visibility for all modes.

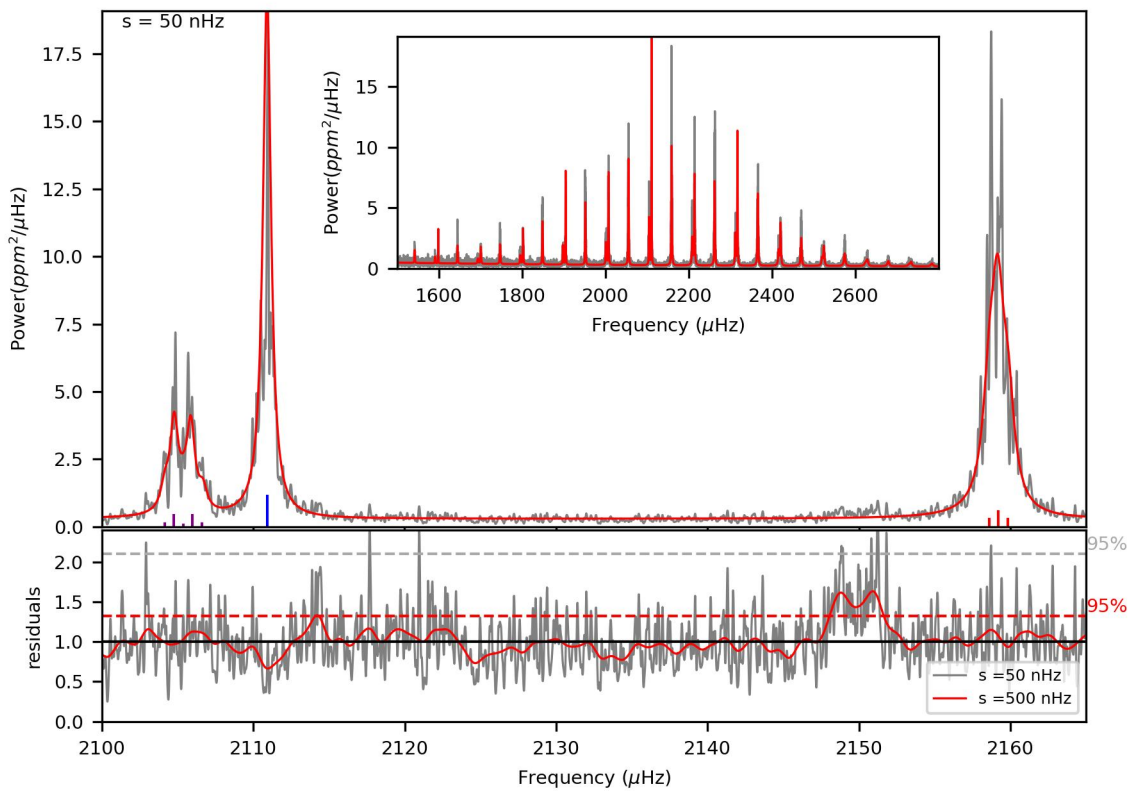


Fig. E.3. Same as Figure E.1 but for 16 Cyg A. Top. Highlight of a $l = 2, 0, 1$ mode group (left to right) and their fit (red). A very mild power asymmetry is seen on the $l = 2$ data. Inset. Overall view of the power spectrum. Bottom. Residual of the fit with two level s of Gaussian smoothing. The residual show an excess of power due to the low HNR ≈ 1.7 $l = 3$ (not fitted here).

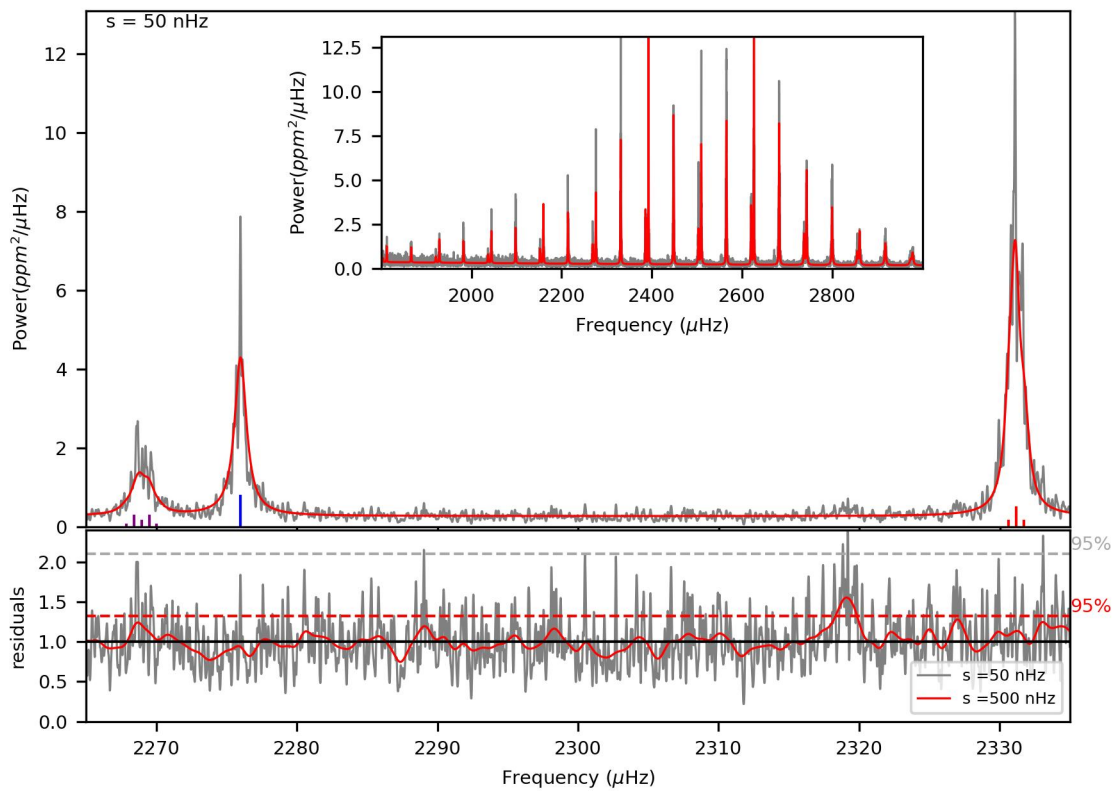


Fig. E.4. Same as Figure E.1 but for 16 Cyg B, $a_4 < -21$ nHz. Top. Highlight of a $l = 2, 0, 1$ mode group (left to right) and their fit (red). A mild power asymmetry is seen on the $l = 2$ data. Inset. Overall view of the power spectrum. Bottom. Residual of the fit with two level s of Gaussian smoothing. The residual show an excess of power due to the low HNR ≈ 1.6 ($l = 3$ not fitted here).

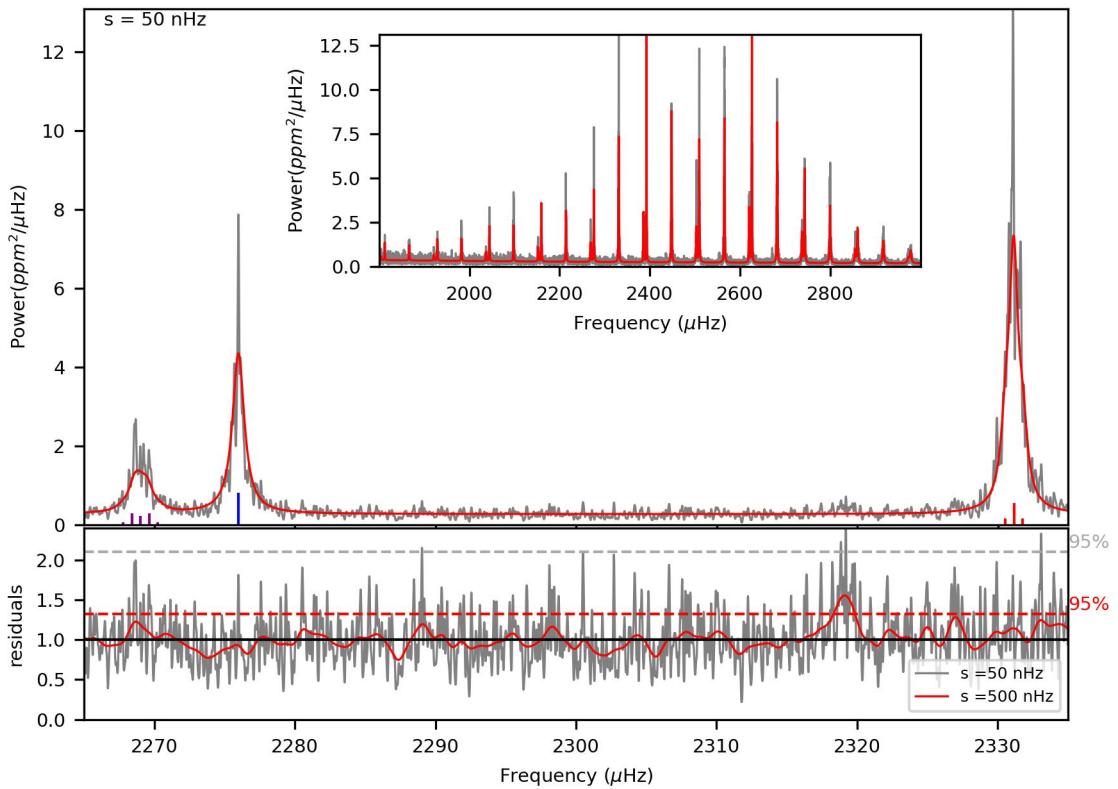


Fig. E.5. Same as Figure E.1 but for 16 Cyg B, $a_4 > -21$ nHz. Top. Highlight of a $l = 2, 0, 1$ mode group (left to right) and their fit (red). Inset. Overall view of the power spectrum. Bottom. Residual of the fit with two level s of Gaussian smoothing. The residual show an excess of power due to the low HNR ≈ 1.6 $l = 3$ (not fitted here).

| | |
|---|-----|
| References | 864 |
| Anderson, E. R., Duvall, Jr., T. L., & Jefferies, S. M. 1990, ApJ, 364, 699 | 865 |
| Antia, H. M., Chitre, S. M., & Thompson, M. J. 2000, A&A, 360, 335 | 866 |
| Appourchaux, T. 2003, A&A, 412, 903 | 867 |
| Appourchaux, T., Antia, H. M., Benomar, O., et al. 2014, A&A, 566, A20 | 868 |
| Appourchaux, T., Gizon, L., & Rabello-Soares, M.-C. 1998, A&AS, 132, 107 | 869 |
| Appourchaux, T., Michel, E., Auvergne, M., et al. 2008, A&A, 488, 705 | 870 |
| Atchadé, Y. F. 2006, Methodology and Computing in Applied Probability, 8, 235 | 871 |
| Baglin, A., Auvergne, M., Barge, P., et al. 2006, in ESA Special Publication, Vol. 1306, ESA Special Publication, ed. | 872 |
| M. Fridlund, A. Baglin, J. Lochard, & L. Conroy, 33 | 873 |
| Ballot, J., Barban, C., & van't Veer-Menneret, C. 2011, A&A, 531, A124 | 874 |
| Bazot, M. 2020, A&A, 635, A26 | 875 |
| Bazot, M., Benomar, O., Christensen-Dalsgaard, J., et al. 2019, A&A, 623, A125 | 876 |
| Bellinger, E. P., Basu, S., Hekker, S., & Ball, W. H. 2017, ApJ, 851, 80 | 877 |
| Benomar, O. 2008, Communications in Asteroseismology, 157, 98 | 878 |
| Benomar, O., Appourchaux, T., & Baudin, F. 2009, A&A, 506, 15 | 879 |
| Benomar, O., Bazot, M., Nielsen, M. B., et al. 2018a, Science, 361, 1231 | 880 |
| Benomar, O., Bedding, T. R., Stello, D., et al. 2012, ApJ, 745, L33 | 881 |
| Benomar, O., Goupil, M., Belkacem, K., et al. 2018b, ApJ, 857, 119 | 882 |
| Benomar, O., Takata, M., Shibahashi, H., Ceillier, T., & García, R. A. 2015, MNRAS, 452, 2654 | 883 |
| Bishop, C. M. 1995, Neural Networks for Pattern Recognition (Oxford University Press, Inc) | 884 |
| Borucki, W. J., Koch, D., Basri, G., et al. 2010, Science, 327, 977 | 885 |
| Brun, A. S. & Browning, M. K. 2017, Living Reviews in Solar Physics, 14, 4 | 886 |
| Buldgen, G., Farnir, M., Eggenberger, P., et al. 2022, A&A, 661, A143 | 887 |
| Buldgen, G., Reese, D. R., & Dupret, M. A. 2015, A&A, 583, A62 | 888 |
| Campante, T. L., Handberg, R., Mathur, S., et al. 2011, A&A, 534, A6 | 889 |
| Campante, T. L., Lund, M. N., Kuszlewicz, J. S., et al. 2016, ApJ, 819, 85 | 890 |
| Catura, R. C., Acton, L. W., & Johnson, H. M. 1975, ApJ, 196, L47 | 891 |
| Ceillier, T., Tayar, J., Mathur, S., et al. 2017, A&A, 605, A111 | 892 |
| Chandrasekhar, S. 1969, Ellipsoidal figures of equilibrium | 893 |
| Chaplin, W. J., Elsworth, Y., Isaak, G. R., et al. 2003, Monthly Notices of the Royal Astronomical Society, 343, 343 | 894 |
| Cochran, W. D., Hatzes, A. P., Butler, R. P., & Marcy, G. W. 1997, ApJ, 483, 457 | 895 |
| Davies, G. R., Chaplin, W. J., Farr, W. M., et al. 2015, MNRAS, 446, 2959 | 896 |
| Deal, M., Richard, O., & Vauclair, S. 2015, A&A, 584, A105 | 897 |
| Deheuvels, S., Doğan, G., Goupil, M. J., et al. 2014, A&A, 564, A27 | 898 |
| Deheuvels, S., García, R. A., Chaplin, W. J., et al. 2012, ApJ, 756, 19 | 899 |
| Deliyannis, C. P., Cunha, K., King, J. R., & Boesgaard, A. M. 2000, AJ, 119, 2437 | 900 |
| Duvall, Jr., T. L., Jefferies, S. M., Harvey, J. W., Osaki, Y., & Pomerantz, M. A. 1993, ApJ, 410, 829 | 901 |
| Dziembowski, W. A., Goode, P. R., Kosovichev, A. G., & Schou, J. 2000, ApJ, 537, 1026 | 902 |
| Farnir, M., Dupret, M. A., Buldgen, G., et al. 2020, A&A, 644, A37 | 903 |
| Frohlich, C., Andersen, B. N., Appourchaux, T., et al. 1997, Sol. Phys., 170, 1 | 904 |
| García, R. A., Hekker, S., Stello, D., et al. 2011a, MNRAS, 414, L6 | 905 |
| García, R. A., Salabert, D., Ballot, J., et al. 2011b, Journal of Physics Conference Series, 271, 012049 | 906 |
| Gehan, C., Mosser, B., Michel, E., Samadi, R., & Kallinger, T. 2018, A&A, 616, A24 | 907 |
| Georgobiani, D., Kosovichev, A. G., Nigam, R., Nordlund, Å., & Stein, R. F. 2000, ApJ, 530, L139 | 908 |
| Gizon, L. 2002, Astronomische Nachrichten, 323, 251 | 909 |
| Gizon, L. 2006, Central European Astrophysical Bulletin, 30, 1 | 910 |

- 911 Gizon, L., Ballot, J., Michel, E., et al. 2013, Proceedings of the National Academy of Science, 110, 13267
 912 Gizon, L., Sekii, T., Takata, M., et al. 2016, Science Advances, 2, e1601777
 913 Gizon, L. & Solanki, S. K. 2003, ApJ, 589, 1009
 914 Gizon, L. & Solanki, S. K. 2004, Sol. Phys., 220, 169
 915 Gough, D. O. & Taylor, P. P. 1984, Mem. Soc. Astron. Italiana, 55, 215
 916 Gough, D. O. & Thompson, M. J. 1990, MNRAS, 242, 25
 917 Gregory, P. C. 2005, Bayesian Logical Data Analysis for the Physical Sciences: A Comparative Approach with ‘Mathematica’ Support
 918 Handberg, R. & Campante, T. L. 2011, A&A, 527, A56
 920 Hansen, C. J., Cox, J. P., & van Horn, H. M. 1977, ApJ, 217, 151
 921 Hartmann, L. & Rosner, R. 1979, ApJ, 230, 802
 922 Harvey, J. 1985, ESA SP, 235, 199
 923 Hogg, D. W., Myers, A. D., & Bovy, J. 2010, ApJ, 725, 2166
 924 Huber, D., Bedding, T. R., Stello, D., et al. 2011, ApJ, 743, 143
 925 Jeffreys, H. 1961, Theory of Probability, 3rd edn. (Oxford, England: Oxford)
 926 Kamiaka, S., Benomar, O., & Suto, Y. 2018, \mnras, 479, 391
 927 King, J. R., Deliyannis, C. P., Hiltgen, D. D., et al. 1997, AJ, 113, 1871
 928 Libbrecht, K. G. & Woodard, M. F. 1990, Nature, 345, 779
 929 Lignières, F., Rieutord, M., & Reese, D. 2006, A&A, 455, 607
 930 Lund, M. N., Lundkvist, M., Silva Aguirre, V., et al. 2014, A&A, 570, A54
 931 Lund, M. N., Silva Aguirre, V., Davies, G. R., et al. 2017, ApJ, 835, 172
 932 Maeder, A. & Meynet, G. 2008, in Astronomical Society of the Pacific Conference Series, Vol. 388, Mass Loss from Stars
 933 and the Evolution of Stellar Clusters, ed. A. de Koter, L. J. Smith, & L. B. F. M. Waters, 3
 934 Maia, M. T., Meléndez, J., Lorenzo-Oliveira, D., Spina, L., & Jofré, P. 2019, A&A, 628, A126
 935 Mathur, S., García, R. A., Régulo, C., et al. 2010, A&A, 511, A46
 936 Metcalfe, T. S., Chaplin, W. J., Appourchaux, T., et al. 2012, ApJ, 748, L10
 937 Metcalfe, T. S., Egeland, R., & van Saders, J. 2016, ApJ, 826, L2
 938 Morel, T., Creevey, O. L., Montalbán, J., Miglio, A., & Willett, E. 2021, A&A, 646, A78
 939 Mosser, B., Goupil, M. J., Belkacem, K., et al. 2012, A&A, 540, A143
 940 Neckel, H. 1986, A&A, 159, 175
 941 Nielsen, M. B., Schunker, H., Gizon, L., Schou, J., & Ball, W. H. 2017, A&A, 603, A6
 942 Nigam, R. & Kosovichev, A. G. 1998, ApJ, 505, L51
 943 Nsamba, B., Cunha, M. S., Rocha, C. I. S. A., et al. 2022, MNRAS[arXiv:2205.04972]
 944 Oláh, K., Kővári, Z., Petrovay, K., et al. 2016, A&A, 590, A133
 945 Oláh, K., Kolláth, Z., Granzer, T., et al. 2009, A&A, 501, 703
 946 Ouazzani, R. M., Marques, J. P., Goupil, M. J., et al. 2019, A&A, 626, A121
 947 Papini, E. & Gizon, L. 2019, Frontiers in Astronomy and Space Sciences, 6
 948 Pijpers, F. P. 1997, A&A, 326, 1235
 949 Pijpers, F. P. 1998, Ap&SS, 261, 17
 950 Ramírez, I., Meléndez, J., & Asplund, M. 2009, A&A, 508, L17
 951 Rauer, H., Catala, C., Aerts, C., et al. 2014, Experimental Astronomy, 38, 249
 952 Ricker, G. R., Winn, J. N., Vanderspek, R., et al. 2014, in Society of Photo-Optical Instrumentation Engineers (SPIE)
 953 Conference Series, Vol. 9143, Proc. SPIE, 914320
 954 Ritzwoller, M. H. & Lavelle, E. M. 1991, ApJ, 369, 557
 955 Roxburgh, I. W. 2017, A&A, 604, A42
 956 Schou, J., Christensen-Dalsgaard, J., & Thompson, M. J. 1994, ApJ, 433, 389
 957 Schuler, S. C., Cunha, K., Smith, V. V., et al. 2011, ApJ, 737, L32
 958 Silva-Valio, A., Lanza, A. F., Alonso, R., & Barge, P. 2010, A&A, 510, A25

| | |
|---|-----|
| Simon, T., Ayres, T. R., Redfield, S., & Linsky, J. L. 2002, ApJ, 579, 800 | 959 |
| Stahn, T. 2010, PhD thesis, Georg August University of Gottingen, Germany | 960 |
| Takeda, Y. 2005, PASJ, 57, 83 | 961 |
| Thompson, M. J., Christensen-Dalsgaard, J., Miesch, M. S., & Toomre, J. 2003, ARA&A, 41, 599 | 962 |
| Toutain, T., Appourchaux, T., Frohlich, C., et al. 1998, in ESA Special Publication, Vol. 418, Structure and Dynamics of the Interior of the Sun and Sun-like Stars, ed. S. Korzennik, 973 | 963 |
| Toutain, T. & Gouttebroze, P. 1993, A&A, 268, 309 | 964 |
| Toutain, T. & Kosovichev, A. G. 2001, in ESA Special Publication, Vol. 464, SOHO 10/GONG 2000 Workshop: Helio- and Asteroseismology at the Dawn of the Millennium, ed. A. Wilson & P. L. Pallé, 123–126 | 965 |
| Ulrich, R. K. 1986, ApJ, 306, L37 | 966 |
| Unno, W., Osaki, Y., Ando, H., Saio, H., & Shibahashi, H. 1989, Nonradial Oscillations of Stars (University Tokyo Press) | 967 |
| van Saders, J. L., Ceillier, T., Metcalfe, T. S., et al. 2016, Nature, 529, 181 | 968 |
| Vaughan, A. H. 1983, in Solar and Stellar Magnetic Fields: Origins and Coronal Effects, ed. J. O. Stenflo, Vol. 102, 113–131 | 969 |
| Verma, K., Faria, J. P., Antia, H. M., et al. 2014, ApJ, 790, 138 | 970 |
| Walker, G., Matthews, J., Kuschnig, R., et al. 2003, PASP, 115, 1023 | 971 |
| White, S. M. 1999, Sol. Phys., 190, 309 | 972 |
| White, S. M., Iwai, K., Phillips, N. M., et al. 2017, Sol. Phys., 292, 88 | 973 |
| White, T. R., Bedding, T. R., Stello, D., et al. 2011, ApJ, 743, 161 | 974 |
| White, T. R., Huber, D., Maestro, V., et al. 2013, MNRAS, 433, 1262 | 975 |